Theses and Dissertations   Student Graduate Works

3-22-2019

Designing Liquid Crystal for Optoacoustic Detection

Michael T. Dela Cruz

DESIGNING LIQUID CRYSTAL FOR OPTOACOUSTIC DETECTION

THESIS

Michael T Dela Cruz, Captain, USAF

AFIT-ENG-MS-19-M-023

DEPARTMENT OF THE AIR FORCE
AIR UNIVERSITY

AIR FORCE INSTITUTE OF TECHNOLOGY

Wright-Patterson Air Force Base, Ohio

The views expressed in this thesis are those of the author and do not reflect the official policy or position of the United States Air Force, Department of Defense, or the United States Government. This material is declared a work of the U.S. Government and is not subject to copyright protection in the United States.

AFIT-ENG-MS-19-M-023

DESIGNING LIQUID CRYSTAL FOR OPTOACOUSTIC DETECTION

THESIS

Presented to the Faculty

Department of Electrical and Computer Engineering

Graduate School of Engineering and Management

Air Force Institute of Technology

Air University

Air Education and Training Command

In Partial Fulfillment of the Requirements for the

Degree of Master of Science in Electrical Engineering

Michael T. Dela Cruz, BS

Captain, USAF

March 2019

DISTRIBUTION STATEMENT A.
APPROVED FOR PUBLIC RELEASE; DISTRIBUTION UNLIMITED.

AFIT-ENG-MS-19-M-023

DESIGNING LIQUID CRYSTAL FOR OPTOACOUSTIC DETECTION

Michael T. Dela Cruz, BS

Captain, USAF

Committee Membership:

Dr. H. Chandrahalim
Chair

Maj T. Laurvick, PhD
Member

Maj N. Herr, PhD
Member

Abstract

This research impacts the development of a cost-saving, on-chip device that can replace a wide range of costly, bulky sensors for commercial and defense applications. In particular, the goals of this work were to design and test a sensor that uses the optical properties of liquid crystal (LC) to detect acoustic waves. This began with developing a method to fine-tune the optical features of the liquid crystal. Statistical analysis of select experimental variables, or factors, lead to ideal settings of those variables when creating the sensor. A two-factor and three-factor experiment were separately conducted and analyzed as a preliminary demonstration of this system. The identification of dominant and ideal factor levels, including their interactions, enabled a statistically enhanced molecular design method of LC for use in many types of sensor applications.

Detecting acoustic waves using the optical properties of a material, or optoacoustic detection, was chosen as the application to test the designed LC. Research continued with analytically calculating the interaction between the soundwaves and the optical and mechanical properties of the LC. Systematic comparisons between a commercially available acoustic sensor system and this theoretical LC optoacoustic detector are provided. Development concluded with a test which demonstrated that ordered, chiral nematic phase of LC can inherently improve an existing acoustic sensing device. Recommendations for further development are discussed.

This work is dedicated to my wife whose never-ending love and support helps me keep my

feet on the ground while encouraging my creative spirit.

Acknowledgments

I would like to express my sincere gratitude to my faculty advisor and committee chair, Dr. Hengky Chandrahalim, for his guidance and support throughout the course of this thesis effort. His insight and experience were undoubtedly appreciated. I would also like to thank Dr. Ling Wang (Texas A&M) for the previous research and providing materials needed for this work. Thank you to the members of my committee, Maj Laurvick (AFIT/ENG) and Maj Herr (AFIT/ENP), for lending their time and expertise in improving the quality of my completed work. In addition, I thank Adam Frizsche and Richard Johnston, without whom I would still be lost in the laboratory. Finally, thank you to Maj Walton and Capt Smith for their work in our initial experiments.

Michael T. Dela Cruz

Table of Contents

List of Figures

x

List of Tables

DESIGNING LIQUID CRYSTAL FOR OPTOACOUSTIC DETECTION

I.   Introduction

1.1.   Impact

"The Air Force must maintain a technological edge over our adversaries by shrewdly seeking out, developing, and mastering cutting-edge technologies—wherever and whenever they emerge."

- Gen Mark A. Welsh III, USAF, Chief of Staff [1]

A common trend with modern cutting-edge technologies is increasing the utility of scarce resources, otherwise known as doing more with less. One way to advance this cause is to reduce the resource cost of acoustic sensors while improving their performance through miniaturization and optimization. As of today, commercially manufactured acoustic detecting devices have a broad range of important applications across multiple frequencies, which include aircraft structural health monitoring [2], early detection of clear-air turbulences [3] and various seismic events [4], submarine communications [5], identification of nuclear detonations [6], ballistocardiography, seismocardiography [7], ultrasound [8] and photoacoustic [9] imaging. This research advances the miniaturization and optimization of sensors by investigating the technology of Optoacoustic Detection (OAD) using liquid crystal (LC). Chapter II, the Literature Review, explores how this technology advances the current state-of-the-art.

1

As a preview, different forms of liquid crystal have specific optical properties that can be observed when light reflects off, or transmits through it. When broadband soundwaves disturb this material, the changes in those optical properties can be observed and converted into an electrical signal, which results in an acoustic transducer device hereafter referred to as an LC optoacoustic detector as detailed in Subsection 3.3.1. Scaling-down and integrating this device on a single chip with corresponding peripheral electronics enables the cost savings benefits of bulk semiconductor manufacturing as well as reducing the sensor's overall size, weight, and power requirements. In contrast, a discrete, unintegrated sound sensing component has a separate manufacturing process from its supporting electronics. As a result, the two components must be integrated together through additional costly processes to create a functional acoustic transducer. Alternative detector designs and prior LC development are discussed in the literature review in Section 2.2 & 2.1, respectively.

1.2. Research

1.2.1. Statistically-Designed Liquid Crystal

The LC sensor research began with two experiments that developed a method to fine-tune the optical features. An Analysis of Variance (ANOVA) statistical method was used in these experiments as a preliminary demonstration to select experimental factors, or variables, which led to ideal settings of those factors when creating the sensor. ANOVA is a known mathematical method in which multiple factors can be changed in a series of experimental runs, and the output determines which of those factors statistically changed a measured experimental result, or observation. An overview of the method, including the

www.manaraa.com

mathematical calculation, is found in Section 3.1.4. Two experiments were separately conducted and each were analyzed via ANOVA: a two-factor (Sections 3.1 and 4.1) and a three-factor experiment (Sections 3.2 and 4.2), where Chapter III is the Methodology, and Chapter 3.5 is Analysis and Results. These analyses enabled the identification of dominant and ideal factor settings, including their interactions. The result was a statistically enhanced method to designing the molecular structure of LC, which can be used in many types of sensor applications including OAD.

1.2.2. *Optoacoustic Detection using Liquid Crystal*

Research continued with the next two phases, theoretical and experimental OAD using LC. The theoretical performance of the device's electrical output was analytically calculated by taking into account the pressure of a soundwave, the optical and mechanical properties of the LC, and test equipment. Section 3.3 explains the calculation of the LC OAD's theoretical response to an acoustic pressure wave when there is an air gap between the acoustic source and the device (free-space coupled) and a white light source is used. The resulting systematic comparisons between a commercially available acoustic sensor and this theoretical LC optoacoustic detector are discussed in Section 4.3. As an incremental design, a LC OAD was created and tested with the acoustic source directly coupled (in contact, no air gap) with the device, which is described in Section 3.4. The results of this experiment are analyzed in Section 4.4. Future work regarding the statistical design method and OAD using LC are presented in Chapter V, Conclusions and Recommendations.

3

1.3. Summary

This research sought out to advance a cutting-edge, economical, compact, and sensitive molecular-based acoustic sensor for use in numerous applications. This began with a method to statistically analyze factors that influence the optical transmission characteristics of LC molecules. Identification of dominant and ideal factor levels, including their interactions, enabled a statistically-enhanced molecular design method of LC. Subsequently, a chip-scale LC optoacoustic sensor was theorized, which had the capability of detecting a range of acoustic signals via free-space coupling using a white light input. Finally, a coupled, or direct contact, version of OAD using LC was tested. This device was used to demonstrate the LC properties, and recommend trajectories for future designs.

II. Literature Review

The purpose of this chapter is to assess the current state-of-the-art of liquid crystal design and acoustic detection. This literature review is divided into two sections. Section 2.1 reviews the design of a specific liquid crystalline phase, and Section 2.2 is an overview of acoustic detection.

2.1. Designing Liquid Crystal
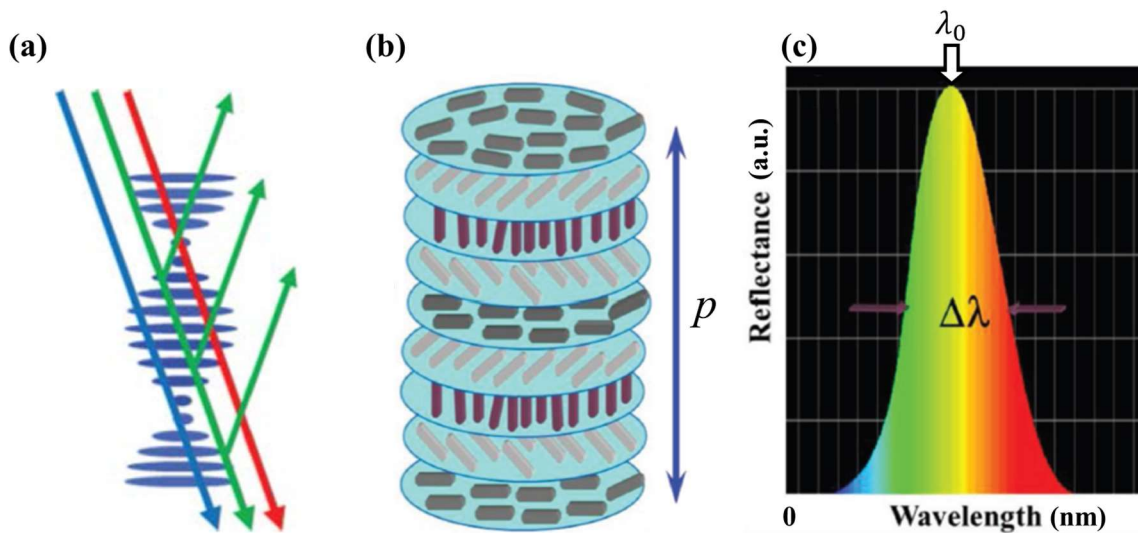
Figure 1. CLC structure and broadband reflection spectrum. (a) Periodically spaced CLC molecules modeled as a Bragg grating that reflect green light in response to an incident broadband light source. (b) Model highlighting helical molecular structures with a helical pitch, p. (c) Theoretical CLC *reflection spectrum* from a broadband white light source with center wavelength, λ_0, and optical reflection bandwidth, $\Delta\lambda$ [10, 11].

Liquid crystal has many uses across commercial, defense, and scientific communities. Specifically, the chiral nematic phase of liquid crystal, or Cholesteric Liquid Crystal (CLC), can be implemented in computer monitors, disposable thermometers, chemical sensors, switchable mirrorless lasers, and adaptive infrared shielding, many of

5

which were inspired by natural phenomena [11]. In this phase, the individual LC molecules orderly form spiraling, helical DNA-like structures. When a thin layer of CLC is contained within an LC cell, such as two parallel glass plates, this system can be modeled as a tunable Bragg grating in Fig. 1 (a). The periodicity of the LC molecules is measured by the pitch, the length-wise distance that the helical structure takes to make a complete 360-degree twist.
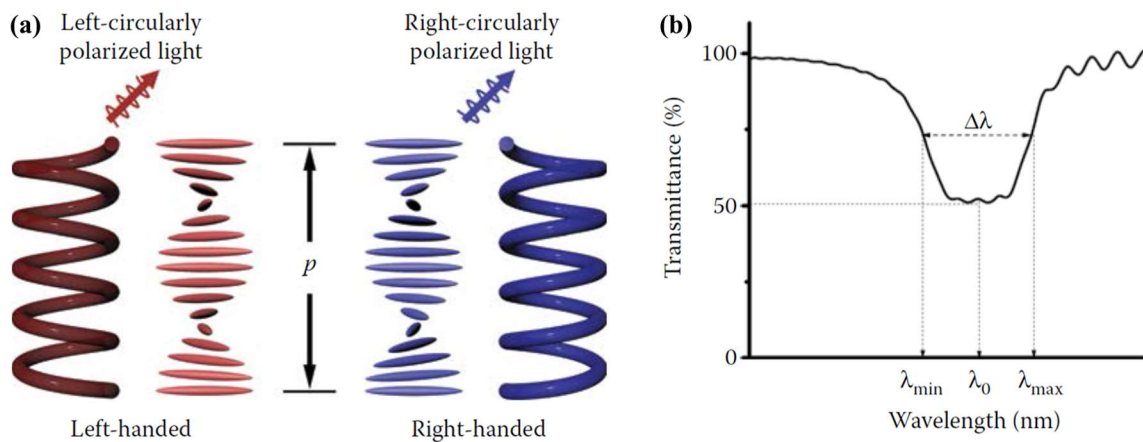
Figure 2. CLC circular light polarization and broadband transmission spectrum. (a) Left-handed and right-handed CLC structures with pitch, p. (b) Theoretical CLC *transmission spectrum* from a broadband white light source with center wavelength, λ_0, and optical transmission bandgap, $\Delta\lambda$ [10].

The optical properties of this system are known such that an incident broadband white light source is selectively reflected as a small band of wavelengths centered on a specific wavelength, the center wavelength illustrated in Fig. 1 (b, c). In addition, the portion of light that follows the same handedness of the CLC structure is reflected and polarized in that same circularly polarized handedness. The oppositely-handed light is transmitted and respectively polarized. Due to polarization, the maximum reflection

6

intensity, or reflectance, at λ_0 is 50%. Conversely, the minimum transmission intensity, or transmittance, at λ_0 is 50%, illustrated in Fig. 2 [10, 11].
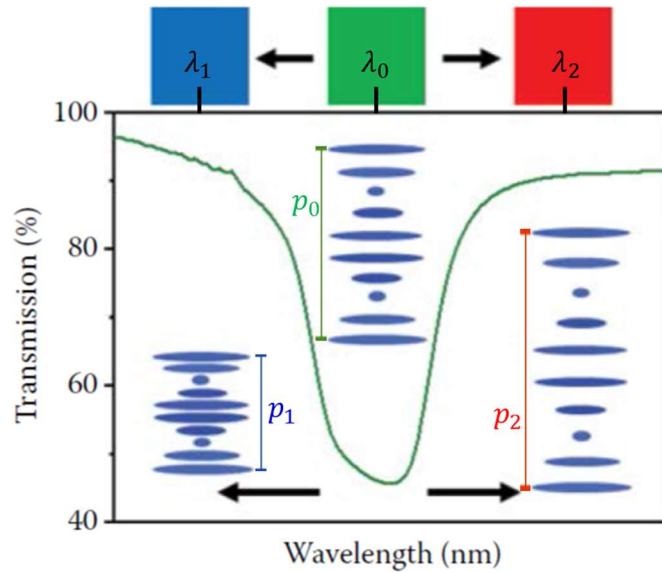
Figure 3. CLC pitch changes resulting in a shifted center wavelength, where $p_1 > p_0 > p_2$ and $\lambda_1 > \lambda_0 > \lambda_2$. The original pitch ($p_0$) corresponds to the green center wavelength (λ_0) and the green plotted line. Shortening the pitch (p_1) results in a shift to a smaller, blue center wavelength (λ_1). A blue-shifted plot is not shown. Increasing the pitch (p_2) results in a shift to a larger, red center wavelength (λ_2). A red-shifted plot is not shown [10].

As a result, the helical pitch of the CLC directly corresponds to its reflected and transmitted properties. The resonant center wavelength changes with the pitch as seen in Fig. 3. Depending on the molecular structure of a given CLC, the swelling of the pitch can result in a longer center wavelength. The constriction of the pitch results in a shorter center wavelength. As a result, this property makes CLC a prime candidate for sensor development, such as, pressure and temperature sensing [10, 12–14].

These properties may be altered through external perturbations. Heating CLC is known to decrease it's viscosity [15]. However, there is a maximum limit to the applied

temperature at which CLC molecules lose the helical structure and become an unorganized, isotropic liquid crystalline phase [16]. This limit varies depending on the chemical structure of the CLC and the method in which it is created. The substrate on which the CLC is deposited also affects the alignment of the helical structure. As a result, glass LC cells include a standard deposition of a thin, clear polymer layer followed by a cloth-rubbing of that polymer. This creates uniform and aligned nanometer-scale grooves which aid in the CLC structure alignment [17]. In addition, properties such as the elastic coefficient of LC can be derived from comparing the viscosity water with that of LC [18, 19].

There are two methods of fabricating CLC. One approach is obtaining liquid crystal molecules that inherently form into the chiral phase as seen in the initial findings of Reinitzer in 1888 [20]. The other method is by dissolving an existing chiral dopant molecule into an achiral nematic LC host [21], which is the focus of this research. Chemists and material scientists characterized, in detail, the fundamental factors that tune and influence this unique material, which include the rubbing direction of an underlying polymer surface [22] and chiral dopant concentration [10].

Currently, extensive statistical studies of these factors primarily occur in the application forefront, such as, identifying factors for defects in liquid crystal displays [23]. Research has also shown techniques that alter the spectral features, such as, the transmission depth and slope. One example is the layering of CLC create bandgap filters that increase the reflectivity, or transmission depth [24]. Broadening of the optical transmission bandgap, or reflective bandwidth, was also achieved through creating a helical pitch that varies along the director by a process of immobilizing layers of LC structures

8

through photopolymerization [10]. However, comprehensive studies that investigate the interactions of the main factors, or variables, which statistically effect the optical spectrum of this thin film of CLC have not received enough attention. This is due to the apparent difficulty of deterministically predicting how the CLC will react to multiple, coinciding intrinsic and external factors.

2.2. Acoustic Detection Overview
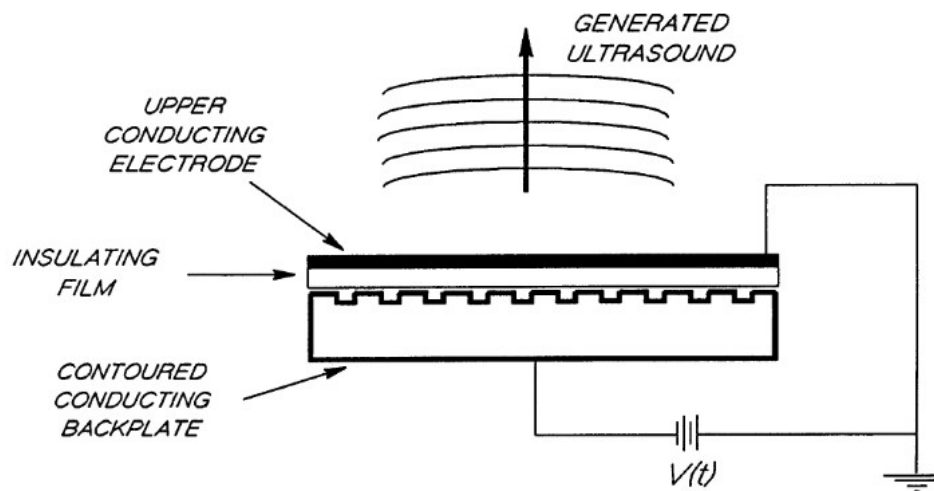
Figure 4. Schematic diagram of a capacitance transducer for the generation and detection of ultrasound in air [25].

Acoustic wave detectors today are primarily dominated by piezoelectric and mechanical-based sensors. Piezoelectric materials have properties such that mechanical deformation of the structure results in an electric field across the material. An applied electric field causes a small deformation of the material. A capacitive transducer, illustrated in Fig. 4, displays the ability to generate acoustic vibrations through modulation of the driving voltage. Alternatively, this can detect vibrations via displacement of the upper conducting electrode, which generates, or transduces, a modulated output voltage, $V(t)$. As

9

acoustic detectors, these methods are highly susceptible to electromagnetic interferences. The frequency detection ranges of piezo- and mechanical-based sensors are defined by the physical dimensions of the sensor materials. In addition, the electrical nature of the sensor depends on larger dimensions for better performance and less noise, which leads to a form factor of approximately 1 cm^2, which is difficult to place on a single chip with supporting electronics [26–28].
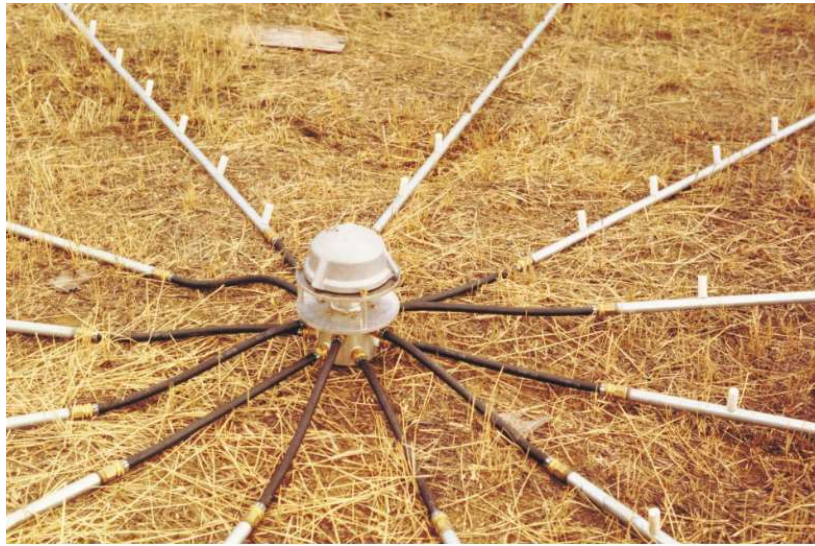
Figure 5. Atmospheric infrasound detector. The main sensor is the center unit of the array. Multiple smaller sensors (vertical white cylinders) are placed at 1-ft intervals from each other radiating out from the center, which enhances the detection of longer wavelengths [29].

Detectors for long acoustic wavelengths, or very low frequencies between 0-20 Hz, demand a very large area [29]. An example of these infrasonic wave detectors are atmospheric infrasound monitors. These require preamplifiers that consume additional space and power to detect acoustic signals. Furthermore, this becomes a drawback when large arrays of these acoustic sensors (Fig. 5) must be integrated in a space-constrained system with a low power requirement. On the other end of the spectrum, ultrasonic waves

have shorter acoustic wavelengths and can be detected by smaller-sized sensors. Ultrasound detection, however, requires an acoustic impedance matching material, such as water, gel, or a solid between the object under test (OUT) and detector. These acoustic impedance matching materials are necessary to reduce the acoustic coupling loss when a soundwave transitions between the OUT and air (or between the detector and air). In addition, at higher frequencies air becomes an increasingly better absorber of acoustic vibrations. Both effects considerably attenuate the intensity of air-coupled soundwaves received by the detector [25, 30, 31].

These acoustic losses complicate ultrasound imaging when the OUT and ultrasound detector must remain contactless, such as, imaging of sensitive wounds or dangerous samples when a dry environment must be maintained [32–35]. Therefore, the development of ultrasensitive free-space, or air-coupled, acoustic detectors are highly desirable to overcome the acoustic coupling and absorption losses.

2.2.1. Optoacoustic Detection

One of the earliest forms of optoacoustic detection was invented in 1880 by Alexander Graham Bell: the photophone. Sunlight was focused onto a silvered plate, or mirror, and a user would speak into the rear of the plate. The reflected output light intensity oscillated at the same frequencies of the verbal acoustic soundwaves that hit the reverse side of the plate. A receiving station converted the light back into audible sound. This was one of Bell's most notable inventions, and it pioneered the bridge between optical and acoustic detections a century before the first generation of fiber optic phone networks [36, 37].

11

Modern optoacoustic detection techniques are appealing alternatives to the conventional soundwave detection methods previously mentioned. These optical-based acoustic detectors do not suffer from geometry-dependent electrical noise, and are immune to electromagnetic interference. The operating frequency of the optoacoustic sensors is not restricted by the physical dimensions of the sensors. As a result, a broadband acoustic sensor can be fabricated on a small substrate. This sensor design allows for the elimination of costly, large, and power-draining preamplifiers while maintaining high sensitivity at a broad frequency range.
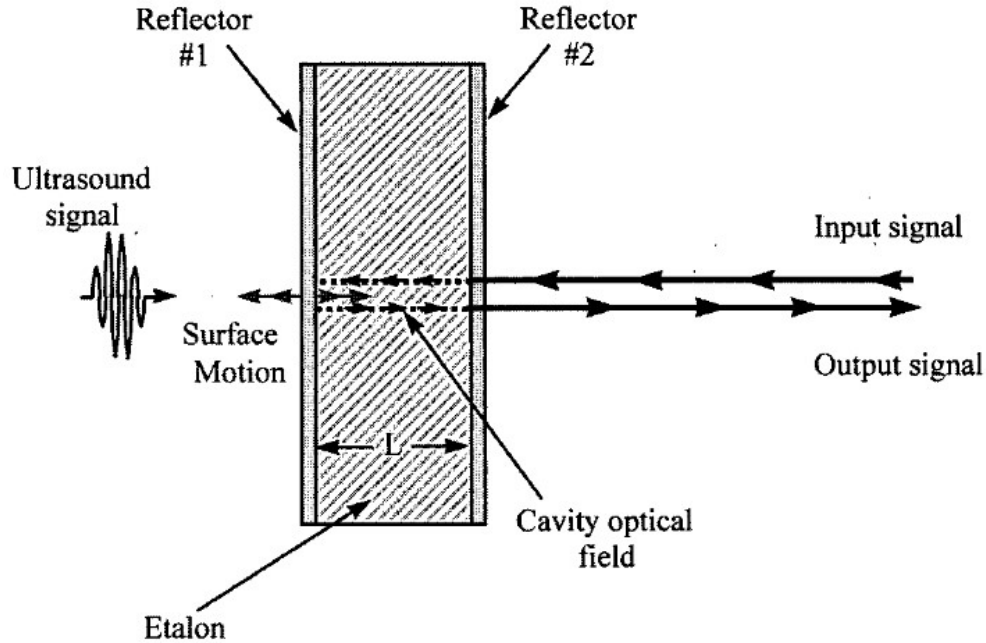
Figure 6. An etalon sensor schematic for detecting ultrasound signals [38].

Optical resonators are one method of achieving optoacoustic detection. Light waves reflect within this cavity such that a characteristic, resonating standing wave, or mode, is created. In this technique, the optical resonator detects soundwaves directly through the photoelastic effect and physical deformation of the cavity, which alters the original

12

resonating wave [39]. Sound is detected by monitoring the modulated output light and comparing it to the input light.

One form of an optical resonator is an etalon, or Fabry-Pérot interferometer, where two parallel translucent plates create the optical resonator shown in Fig. 6. Incident light from an external source enters the etalon and undergoes multiple beam interference, where light waves interact constructively and deconstructively. This produces reflected and transmitted outputs beams. The same phenomena occurs in thin-film interference [40], such as, the spectrum of colors reflected from soap bubbles or oil on concrete. The reflected beam is typically used as the output due to the placement of the detector against the object being tested, which creates a difficult configuration to view the transmission output. The intensity and wavelength at the output depends on both the distance the light beam traveled (optical path length) within the resonator and the optical wavelength. Presently, these were studied for use in ultrasound detection, photoacoustic imaging, and photothermal probes for use in the biomedical field with varying efficiencies [38, 41, 42]. However, these implemented lasers with bulky and expensive external equipment as the optical source. This research includes a white light source to reduce the overhead weight and resource costs to improve upon this design.

Over the past decade, various optical ring resonators have been developed as optoacoustic detectors, including polymer ring resonators on a chip (Fig. 7) [43–46], silicon/silicon nitride ring resonators on a thin membrane [47, 48], and fused silica microresonators [49]. Due to the high optical efficiency, measured as the quality-factor (Q-factor), of the whispering gallery mode (WGM), the ring resonator can achieve high

13

pressure sensitivity. Ring resonators have a small form factor (typical ring diameter: 30–200 μm), which is beneficial in building an array of detectors on a microscopic platform. However, most current acoustic detection experiments using WGM ring resonators are performed in an aqueous environment due to better acoustic transmission through liquids as opposed to air. Scientists recently demonstrated an air-coupled ultrasound detector using high Q-factor ($>10^7$) ring resonators based on fused silica capillaries. These optical ring resonators were able to detect ultrasound waves up to 800 kHz [39]. However, the light coupling mechanism using tapered fiber optics is impractical for many applications, and infrasound. Furthermore, bulky and expensive tunable lasers were necessary to obtain whispering-gallery resonances. Finally, the rigid fused-silica material was only modestly deformed due to acoustic stimulation [50, 51].
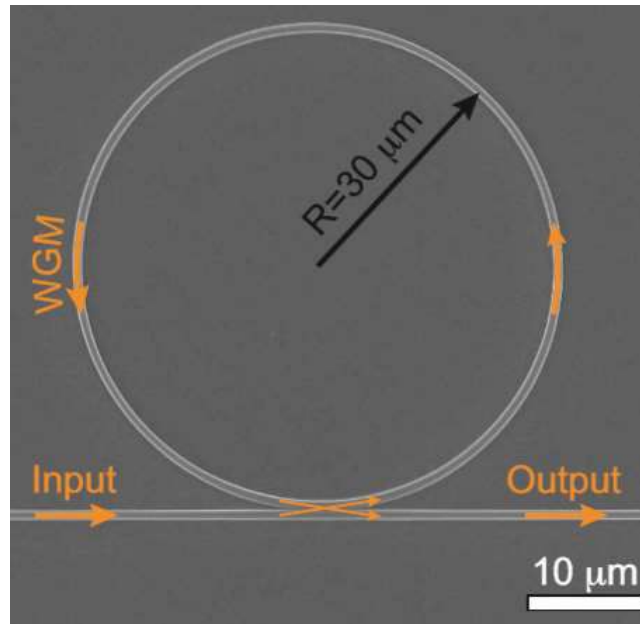
Figure 7. Polymer ring resonator design imaged by Scanning Electron Microscope (SEM). The arrows display the path of light [44].

14

2.3. Summary

Liquid crystal has been integrated into many display and sensor technologies. Over a century of research has defined the behavior and creation of the helical CLC structure. Individual variables that affect its properties are known. However, it is difficult to predict or model a CLC response when there are many coinciding stimuli present.

Modern acoustic detection technology relies on piezoelectric and mechanical technology in which their size and sensitivity are well developed. These have various issues ranging from geometry-dependent electrical noise, electromagnetic interference, and acoustic coupling and absorbing losses. Optoacoustic detection does not depend on geometry to sense acoustic signals. An etalon and ring resonator sensor were presented as existing OAD methods.

15

III. Methodology

This chapter explains the steps taken during each of the four parts of this research. Section 3.1 details the two-factor statistical design experiment that emphasized preparation of thin-film CLC. Section 3.2 repeats steps from the previous section but with three factors that emphasized environmental conditions. Section 3.3 explores the theoretical calculation of how the LC optoacoustic detector would respond to soundwaves. Section 3.4 describes the procedures of the LC OAD experiment.

3.1. Two-Factor Statistical Design Experiment

The following details the process of this experiment with four subsections. The overview of how and why the statistical method was used is elaborated in the following, Subsection 3.1.1. Reasoning behind the chosen main factors, or variables, of the experiment and their associated levels, or settings, are found in Subsection 3.1.2. The steps to the overall experimental process are described in Subsection 3.1.3. Lastly, an in-depth statistical calculation was isolated in Subsection 3.1.4 as a reference for the mathematical algorithm.

3.1.1. Statistical Method

The statistical method in this thesis used the wealth of prior research, per the previous chapter, to aid in engineering a liquid crystalline-based molecular system. This method enabled the understating of main variables, or factors, and their interactions with each other that statistically affected the features of the chiral nematic liquid crystal phase. An Analysis of Variance (ANOVA) statistical calculation was used as a proof-of-concept to find the significant factors and interactions that change the slope of the optical bandgap

16

shown in Fig. 8 (c). A detailed ANOVA calculation is described in Subsection 3.1.4. An

interaction or factor that was identified as significant connotated that there was enough
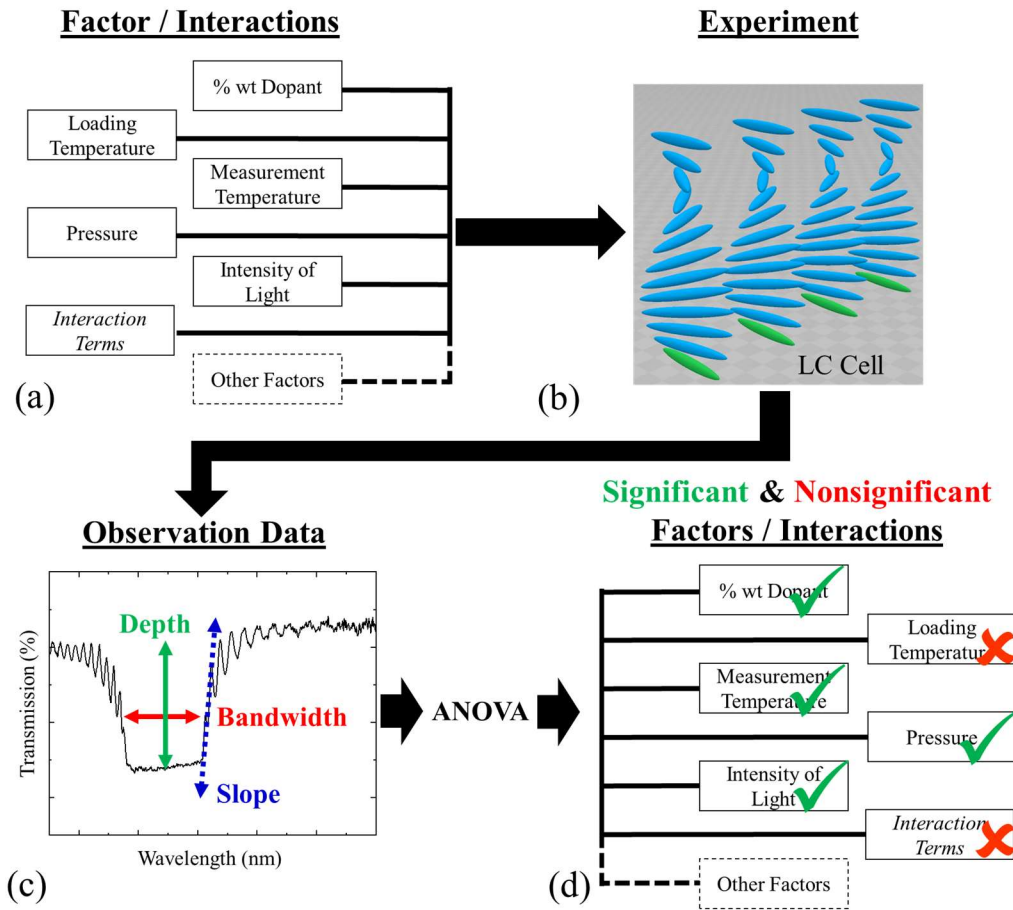
Figure 8. Example flow chart of statistically-assisted design of LC molecular systems. (a) Factors with

interactions were chosen based on available research. (b) Factors were varied to different levels based on

statistical design theory. (c) Observation data of the LC's optical transmission characteristics were

recorded. (d) ANOVA output identifies significant and nonsignificant factors and interactions.

evidence such that variation of an observed measurement was caused by that factor. The

magnitude of this evidence was simplified as a percentage value, or *p-value*, which is a

positive real number that ranges between zero and one. A smaller p-value suggested greater

evidence that a factor or interaction was significant to the variation of an observed

17

measurement. Conventionally, a p-value less than 0.05 identifies a factor as significant. However, it should be noted that a smaller level of significance can be used if decisions implicated by the experiment involve greater risks [52], such as human safety systems and nuclear reactor tests.
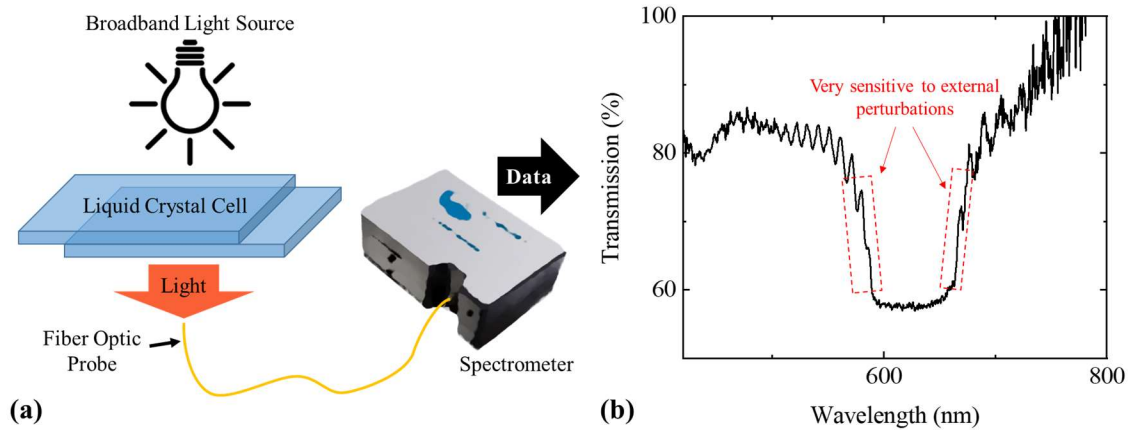
Figure 9. Measurement of the LC optical spectrum. (a) Illustration of the process used to identify the optical resonance of the LC cell. (b) A sample of the measured optical resonance of the LC cell.

The outputted ANOVA p-values were derived from a partitioning of the total observed variability into its component parts [52]. As a result, each main factor and their interactions were separately evaluated for whether or not it significantly affected the variability of the observed, or measured, phenomena. A simplified flow chart of the process with example factors is displayed in Fig. 8. In this experiment, the chosen measured observation was the slope of the optical bandgap edge in the broad spectrum of a thin-film CLC as highlighted in Fig. 9. The unit of measurement was percent transmission per wavelength (%transmission / nanometer). This observation was an important factor for the design of an LC OAD. Further reasoning behind this decision is found in the theoretical calculations of the detector in Section 3.3. The design of this experiment also optimized

18

the number of runs, material, and resources needed for an experiment. In addition, ideal factor level settings were empirically identified through observed measurements of multiple samples.

3.1.2. *Factors and Their Levels*

The factors in this statistical experiment emphasized how the CLC was prepared. The first main factor chosen for the experiment (factor A) was the dopant concentration due to its known direct correlation to the helical shape of the CLC, which enables the Bragg grating phenomenon per Section 2.1. Four levels, or settings, of the dopant concentration factor were chosen as: 0%, 1.80%, 2.05%, and 2.56% weight of dopant in the LC-dopant mixture. A 0% weight dopant was undoped achiral LC, which was used as a control level. The 1.80% weight dopant was selected since it shifted the optical bandgap to a wavelength that was the upper wavelength boundary of the spectrometer's light source. Any lower percent weight of dopant would result in an optical bandgap outside the optimal range of the white light source, which would distort the spectrometer's transmission measurement. A 2.56% weight dopant shifted the optical bandgap to a wavelength that was the lower wavelength boundary of the spectrometer light source. A higher percent weight of dopant would result in an optical bandgap outside the range of the white light source. These noisy high and low wavelength boundaries are shown in Fig. 11. The 2.05% weight dopant was chosen as an intermediary level.

The second factor (factor B) was the temperature of the LC cell at the time it was loaded with CLC. The loading temperature was chosen as a factor of interest since it was observed that heating CLC lowered its viscosity, per Section 2.1, resulting in shorter time

19

spent while loading, and it was unknown if this significantly affected the LC cell construction which may then change CLC performance. The two levels for the loading temperature factor were room temperature and 103.9°C. These temperatures captured the full range of upper and lower experimental temperature boundaries. The lower boundary was the lowest temperature achievable without a cooling element. The upper boundary was the observed average temperature at which CLC changed from cloudy to clear, which signified the unorganized isotropic phase of the liquid crystal per Section 2.1.
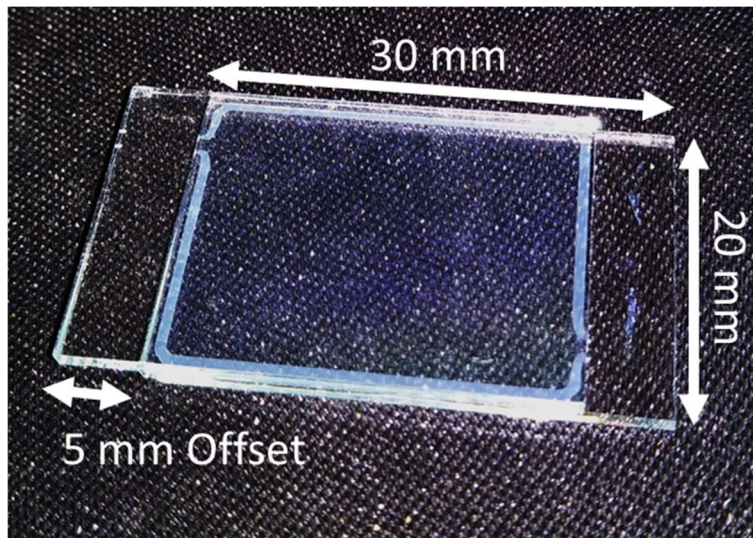
Figure 10. An empty LC cell of which the dimensions of the stacked glass plates and their offset are displayed. The adhesive layer frames the LC cell in a white border, and includes two inlet/outlet openings on the top left and bottom right.

The commercially purchased LC cell consisted of two separate 30 x 20 x 1 mm glass plates stacked on each other with a 5 mm offset. The inside faces of the plates were prepared with the standard polymer deposition and cloth-rubbing process, which aids in CLC structure alignment as discussed in Section 2.1. Those inside faces of the plates were adhered together along the edges such that a 3 μm cavity was maintained between the

20

plates. Construction of the cell included an inlet and outlet opening where the adhesive layer was not deposited. These gaps in the adhesion, in conjunction with the offset glass plates, enabled the loading, or injecting, of mixed CLC into the LC cells.
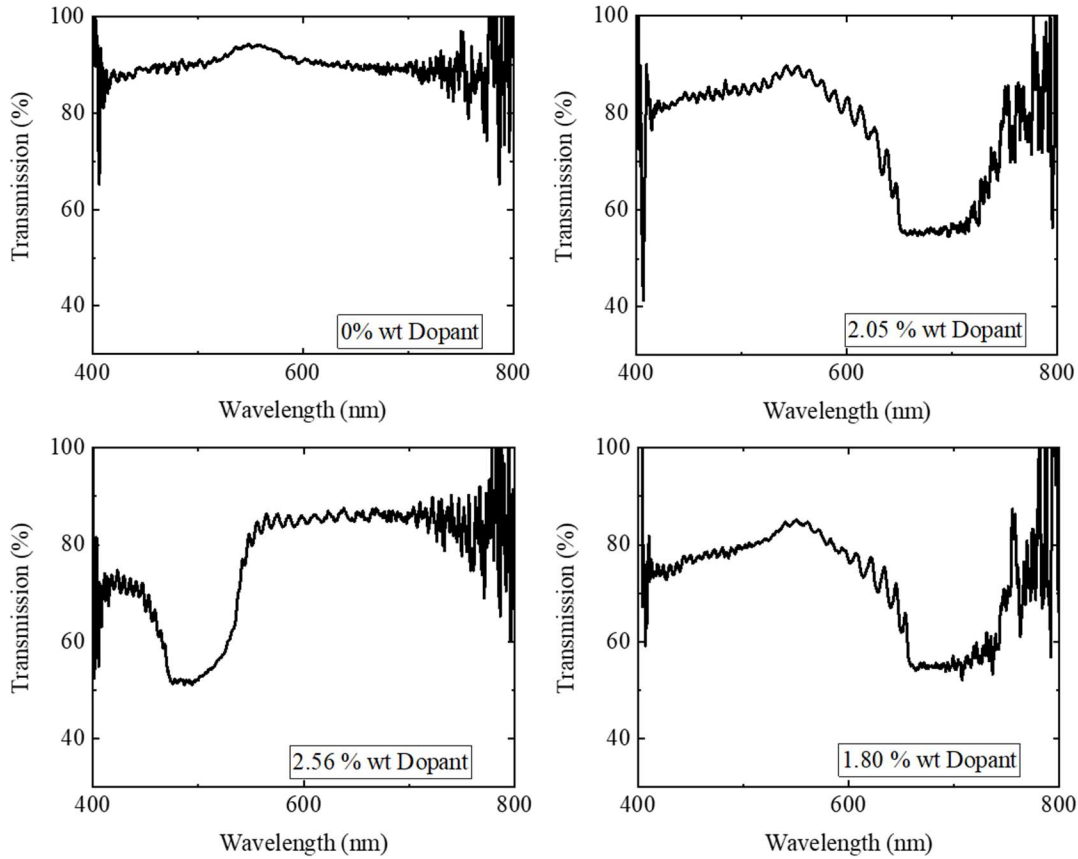
Figure 11. Representative sample of the measured CLC spectra featuring the four levels of percent weight of dopant illustrating the range of wavelengths measurable when determining dopant concentration values.

The experiment was planned to be conducted twice to account for LC cell defects as a difficult to control factor, or nuisance factor. These two replicate experiments allowed for the ANOVA calculation to examine if the LC cells used in each replicate significantly contributed to the optical bandgap slope. These defects may include variability of the index of refraction, the gap between the glass plates, defects in the glass or gap, and other optical

21

properties. These decisions resulted in two temperatures and four dopant concentrations which yielded eight LC cells that accounted for all combinations of temperature and dopant levels. The two replicate experiments, each with eight LC cells, brought the total to 16 LC cell combinations that completed the overall experiment as seen in Table 1.

Table 1. Design of the two-factor experiment with un-coded levels. The observation column is populated in the analysis and results, Chapter IV (Table 5).

Run	Cell ID #	Factor A: Loading Temperature	Factor B: Dopant (%wt)	Replicate #	Observation: |Avg. Slope| (%trans. / nm)
1	14	Room	0	1	
2	15	Room	1.08	1	
3	16	Room	2.05	1	
4	17	Room	2.56	1	
5	18	103.9°C	0	1	
6	19	103.9°C	1.08	1	
7	20	103.9°C	2.05	1	
8	21	103.9°C	2.56	1	
9	22	Room	0	2	
10	23	Room	1.08	2	
11	24	Room	2.05	2	
12	25	Room	2.56	2	
13	26	103.9°C	0	2	
14	27	103.9°C	1.08	2	
15	28	103.9°C	2.05	2	
16	29	103.9°C	2.56	2	

3.1.3. Experimental Process

The experiment consisted of two phases: the loading of CLC into the LC cells and the spectral measurement of the loaded LC cells. Prior to loading, four glass vials were previously prepared with each one containing one of the four CLC mixtures, which

consisted of the unorganized, achiral nematic LC (4-Cyano-4'-pentylbiphenyl) and a chiral dopant (R5011). The loading phase began with heating a hotplate to the upper temperature limit, 103.9°C. The four full vials and four empty LC cells were placed on the hotplate.
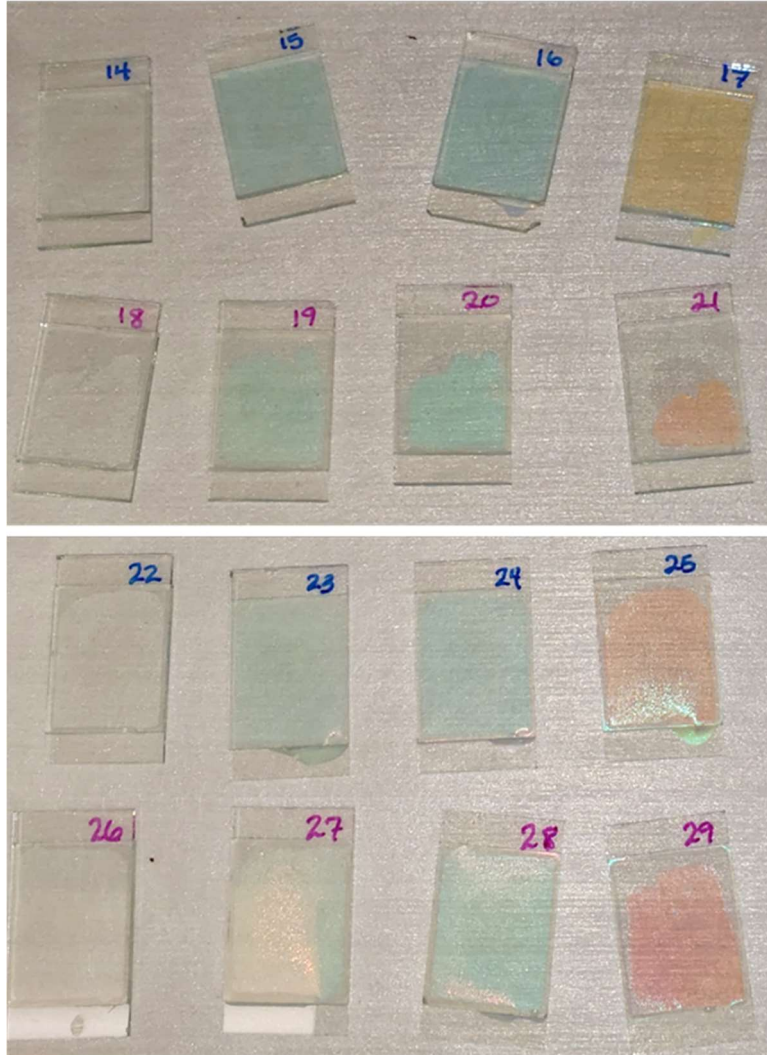
Figure 12. CLC thin-films in LC cells: (Top) The first experimental replicate. (Bottom) The second experimental replicate. Blue markings indicate room loading temperatures. Purple markings indicate 103.9°C loading temperatures. Numbers are for cell identification, and were continued from prior experiments. CLC colors are due to transmission of light from the white background through the LC cell to the observer. Reflected output light is readily seen on #25, #27, and #28.

23

These vials were heated approximately five minutes in order to reach a stable temperature. At the same time, an additional set of four empty LC cells were placed on the test bench table at room temperature away from the hotplate. Once the CLC mixtures turned clear in the vials, a pipette was used to load a mixture into one LC cell on the hotplate and a one cell at room temperature. The loading was repeated for the rest of the mixtures using a clean pipette per mixture. After all eight cells were loaded, the four mixtures and the four loaded LC cells were removed from the hotplate and allowed to cool, which completed the loading of the first replicate experiment.

This created eight loaded LC cells that satisfied every combination of temperature and dopant levels: four hot-loaded cells and four room-temperature-loaded cells (Cell ID #14-21). The mixtures were allowed to cool for 15 minutes, then the same steps were replicated for the second loading set (Cell ID #22-29), which completed the loading phase for all 16 CLC thin-films as seen in Fig. 12 above. All tasks were accomplished by the same individual in both replicate loading sets to eliminate variability between multiple experimenters as a factor.

The spectral measurement phase consisted of capturing optical data through a spectrometer using its transmission mode pictured in Fig. 13. The spectrometer was an Ocean Optics FLAME-S-VIS-NIR-ES, which covered the visible wavelength range of the experiment. Data was analyzed with the MATLAB code in Appendix A. white light emitting diode lamp used as the light source. The necessary background calibrations were conducted before the measurement a new LC cell. One measurement of an LC cell resulted in a percent transmission versus wavelength spectrum plot similar to Fig. 11. Optical

24

bandgap slopes were defined as percent transmission per wavelength (in nanometers). For each LC cell, three spectral measurements of that cell were captured in random locations. This accounted for variability in CLC alignment and dopant concentration across a single cell.
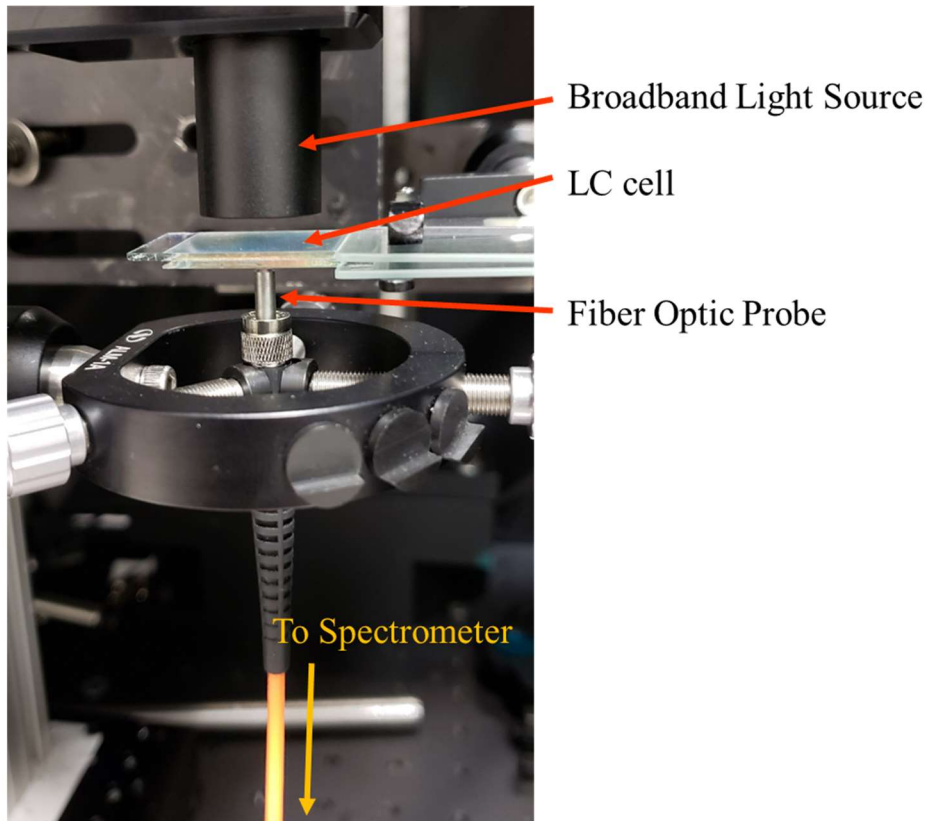
Figure 13. Configuration of equipment for the two-factor experiment.

Each spectrum was analyzed via a custom MATLAB algorithm (Appendix B) to find the steepest slope created by the edges of the optical transmission bandgap. This was done to create a consistent, repeatable process when analyzing the data to further eliminate variability between multiple experimenters. The three identified slopes were averaged together to obtain the final slope result for a single LC which was inputted into Table 1. An absolute value was used since the sign of the slope measurement is irrelevant to the

slope's magnitude. This process was repeated for all 16 LC cells. The observation data was inputted into statistical software, Minitab 17, to calculate the ANOVA and determine the factors and interactions that were significant in changing the optical bandgap slope (Section 4.1).

3.1.4. ANOVA overview

Table 2. A two-factor, mixed-level design with coded factor levels and observation notation that corresponds to the values in Table 1.

Run	Factor A Levels	Factor B Levels	Replicate #	Observation (y_{ijk})
1	1	1	1	y_{111}
2	1	2	1	y_{121}
3	1	3	1	y_{131}
4	1	4	1	y_{141}
5	2	1	1	y_{211}
6	2	2	1	y_{221}
7	2	3	1	y_{231}
8	2	4	1	y_{241}
9	1	1	2	y_{112}
10	1	2	2	y_{122}
11	1	3	2	y_{132}
12	1	4	2	y_{142}
13	2	1	2	y_{212}
14	2	2	2	y_{222}
15	2	3	2	y_{232}
16	2	4	2	y_{242}

The following calculation followed after collecting the observation data. Only the statistical theory used for this specific case is presented in this thesis. Minitab 17 was used as the statistical software application. Other applications are widely available to verify these mathematical calculations. Per the previous section, the following assumes that *factor*

26

A (loading temperature) has two *levels*, *factor B* (dopant concentration) has four *levels*, and that the eight LC cell experiment was conducted twice (two *replicates*). This is described as a two-factor, mixed-level design due to the two factors each having an amount levels that do not equal each other [52].

Each experimentally measured value, or *observation*, from an experiment can be described by a host of different equations, or models, that explain how factors influence the variation of the observation. The *effects model* was chosen for this, which shows the cumulative effect these pieces have on an observation by splitting up the factor and interaction effects into a sum of terms.

Let each measured observation be represented as y_{ijk}. The ijk notation identifies which factor levels and replicates correspond to that observation as seen in Table 2. The variable i defines the level of factor A, where $i = (1, \dots, a)$, and a is the general case of the number of levels in factor A. The j defines the level of factor B, where $j = (1, \dots, b)$, and where b is the general case of the number of levels in factor B. The variable k defines the replicate number, where $k = (1, \dots, n)$, and n is the general case of the number of replicates. The effects model is then defined as, $y_{ijk} = \mu + \tau_i + \beta_j + (\tau\beta)_{ij} + \varepsilon_{ijk}$, where μ is the overall mean effect, τ_i is the effect of the ith level of factor A, β_j is the effect of the jth level of factor B, $(\tau\beta)_{ij}$ is the effect of the ijth interaction between τ_i and β_j, and ε_{ijk} is random error that not is attributed to the previous terms.

The following variables are defined: $y_{i..}$ is the sum of all observations under an ith level of factor A (For example, using Table 2, $y_{1..} = y_{111} + y_{121} + y_{131} + y_{141} + y_{112} + y_{122} + y_{132} + y_{142}$.); $y_{.j.}$ is the sum of all observations under a jth level of factor B; $y_{ij.}$ is

27

the sum of all observation in an ijth interaction; and $y_{...}$ is the total sum of all the observations. Their averages are defined as the variables $\bar{y}_{i..}$, $\bar{y}_{.j.}$, $\bar{y}_{ij.}$, and $\bar{y}_{...}$, respectively.

Assuming that the data follows a statistically normal distribution, consists of independent random variables, and has constant variance, the experimental sample variance (S^2), a standard measure of variability, of the observed data is

$$S^2 = \frac{SS_T}{N-1}, \tag{1}$$

where SS_T is the total corrected *sum of squares* and N is the total number of observations. Methods exist to verify the assumptions, but are not covered in this overview. This total sum of squares is a mathematical method used as a measure of overall variability, and is the vehicle in which ANOVA partitions the variance of a data set into its component parts. SS_T can be written as

$$\sum_{i=1}^{a}\sum_{j=1}^{b}\sum_{k=1}^{n}\left(y_{ijk} - \bar{y}_{...}\right)^2$$

$$= \sum_{i=1}^{a}\sum_{j=1}^{b}\sum_{k=1}^{c}\left[(\bar{y}_{i..} - \bar{y}_{...}) + (\bar{y}_{.j.} - \bar{y}_{...}) + (\bar{y}_{ij.} - \bar{y}_{i..} - \bar{y}_{.j.} + \bar{y}_{...})\right.$$

$$\left. + (y_{ijk} - \bar{y}_{ij.})\right]^2$$

$$= bn\sum_{i=1}^{a}(\bar{y}_{i..} - \bar{y}_{...})^2 + an\sum_{j=1}^{b}(\bar{y}_{.j.} - \bar{y}_{...})^2$$

$$+ n\sum_{i=1}^{a}\sum_{j=1}^{b}(\bar{y}_{ij.} - \bar{y}_{i..} - \bar{y}_{.j.} - \bar{y}_{...})^2 + \sum_{i=1}^{a}\sum_{j=1}^{b}\sum_{k=1}^{n}(y_{ijk} - \bar{y}_{ij.})^2. \tag{2}$$

28

The partitioned sections are the four terms found on the right-hand side of this equation. Those terms are defined as the sum of squares due to factor A (SS_A), the sum of squares due to factor B (SS_B), the sum of squares due to the interaction between A and B (SS_{AB}), and a sum of squares due to random error (SS_E), respectively. This is simplified to the equation below.

$$SS_T = SS_A + SS_B + SS_{AB} + SS_E \tag{3}$$

Table 3 summarizes the remaining equations. The *degrees of freedom* are the number of independent elements in the sum of squares. The degrees of freedom are also the divisors in the *mean square* calculation. Note that ANOVA tables calculated with more sources of variation (more factors and interactions) the calculation of a mean square is limited by the degrees of freedom. More sources of variation can reduce the degrees of freedom to zero, which in turn disables the calculation of MS_E and F_0. This can be mitigated by omitting certain sources of variation in the table if there is a scientific reasonable doubt that the source does not contribute to variation, which is used in blocking.

Blocking is a design technique used to improve precision when deciding which factors of interest are to be compared. This is used to reduce or eliminate sources of variation that are inherently difficult to control, known as nuisance factors. In this paper, a second ANOVA was recalculated in the results to include replicates as a blocking factor, which represented the source of variation due to defects in LC cells. This mathematical algorithm adds a third factor, but leaves out the additional interactions. This is similar to the two-factor ANOVA, but is not detailed here. The additional interaction terms were not included due to the degree of freedom limitation previously discussed.

29

Finally, F_0 is used to calculated the p-value. This can be done using statistics software applications, a table of values containing the percentage points of the F Distribution, or various modern scientific calculators. Any method only requires knowing the degrees of freedom in the numerator and denominator of F_0 as well as its final value. For example, $F_0 = 0.03$ for factor A on the table below. The degrees of freedom for the numerator and denominator are 1 and 8, respectively. This yields a p-value of 0.863.

The process of determining if an effect has a significant impact on the variation now depends on hypothesis testing of the effect terms. To review hypothesis testing, the *null hypothesis* (H_0) takes the standpoint that a factor or interaction effect term does not affect the variability of the observation. When the null hypothesis is rejected, an opposing, or *alternative hypothesis* (H_1), is assumed correct until disproven with future research.

Table 3. ANOVA table equations for a fixed effects model, two-factor experiment with the interaction term included [52]. The evaluated table is found in Section 4.1, Table 6.

Source of Variation	Sum of Squares	Degrees of Freedom	Mean Square	F_0
Factor A	SS_A	$a - 1$	$MS_A = \dfrac{SS_A}{a-1}$	$F_0 = \dfrac{MS_A}{MS_E}$
Factor B	SS_B	$b - 1$	$MS_B = \dfrac{SS_B}{b-1}$	$F_0 = \dfrac{MS_B}{MS_E}$
Interaction (A & B)	SS_{AB}	$(a-1)(b-1)$	$MS_{AB} = \dfrac{SS_{AB}}{(a-1)(b-1)}$	$F_0 = \dfrac{MS_{AB}}{MS_E}$
Error	SS_E	$ab(n-1)$	$MS_E = \dfrac{SS_E}{ab(n-1)}$	
Total	SS_T	$abn - 1$		

For this study, H_0 is the assumption that a factor or interaction effect term does not contribute to the variability of y_{ijk}. For τ_i, this is defined as $H_0: \tau_1 = \tau_2 = 0$. For β_j, this

is defined as $H_0: \beta_1 = \beta_2 = \beta_3 = \beta_4 = 0$. For $(\tau\beta)_{ij}$, this is defined as $H_0: (\tau\beta)_{ij} = 0$ for all i, j. Alternatively, H_1 is the assumption that at least one factor or interaction effect term contributes to the variability of y_{ijk}. For τ_i, this is defined as H_1: at least one $\tau_i \neq 0$. For β_j, this is defined as H_1: at least one $\beta_j \neq 0$. For $(\tau\beta)_{ij}$, this is defined as H_1: at least one $(\tau\beta)_{ij} \neq 0$. It is the researcher's burden to provide significant proof to reject, or disprove, only the null hypothesis.

This level of significance brings us back to the *p-value*, a measure of the weight of evidence against H_0. The p-value is compared against the smallest level of significance needed to reject the null hypothesis, which is 0.05 per Subsection 3.1.1. H_0 is rejected when the p-value is less than the chosen level of significance. Logically, H_1 is then assumed to be true until proven otherwise, which means that at least one of the effect terms is nonzero and contributes to variation. As a result, the factor, or interaction, is identified as significantly contributing to overall variance of the measured experimental observations. In addition, labeling significant sources of variation must follow a hierarchy, whereas a main factors significance is masked by that of a higher-order interaction that main factor falls under. For example, if second-order interaction between factor A and B is labeled significant, the individual main factors cannot be labeled significant no matter their p-value due to the structural hierarchy of the statistical design. In effect, a significant interaction masks its lower-order main factors [52].

3.2. Three-Factor Statistical Design Experiment

Research shifted into a separate, refined three-factor analysis. The statistical procedure of this experiment was the same as previously explained in the two-factor experiment, Subsection 3.1.1. The following sections only review how the three factors and their levels were chosen (Subsection 3.2.1), and the experimental process (Subsection 3.2.2).

3.2.1. Factors and Their Levels

The factors in this statistical experiment emphasized the environmental conditions around the CLC during spectral measurement. The first main factor chosen for the experiment (fact or A) was the temperature of the LC cell during the spectral measurement. The measurement temperature was chosen as a second factor of interest since heating CLC directly governs the helical pitch of the its structure, which results in a color shift of the transmitted resonant, center wavelength per Section 2.1. The two levels for the measurement temperature factor were room temperature and 55°C. These temperatures captured the full range of upper and lower experimental temperature boundaries. The lower boundary was the lowest temperature achievable without a cooling element. The upper limit was the highest and safest temperature that the vacuum chamber seals could withstand without failing.

The second factor (factor B) was the pressure exerted on the LC cell during measurement. The physical pressure, or strain, on the helical CLC structure affects the pitch causing a color shift in the transmission spectrum per Section 2.1. The two levels were governed by the vacuum chamber and laboratory conditions. The upper boundary was

32

the pressure at room temperature, ground altitude in Dayton, Ohio, which was recorded as 99 kPa. The lower boundary was 14 kPa due to the physical limits of the vacuum pump and vacuum chamber seals.

Table 4. Design of the three-factor experiment. The observation column is populated in the analysis and results, Chapter IV (Table 9).

Run	Factor A: Measurement Temperature	Factor B: Pressure (kPa)	Factor C: Dopant (%wt)	Replicate # (Batch) [Cell ID#]	Observation: |Avg. Slope| (%trans. / nm)
1	Room	14	1.08	1 [#17]	
2	Room	14	2.56	1 [#15]	
3	Room	99	1.08	1 [#17]	
4	Room	99	2.56	1 [#15]	
5	55°C	14	1.08	1 [#17]	
6	55°C	14	2.56	1 [#15]	
7	55°C	99	1.08	1 [#17]	
8	55°C	99	2.56	1 [#15]	
9	Room	14	1.08	2 [#25]	
10	Room	14	2.56	2 [#23]	
11	Room	99	1.08	2 [#25]	
12	Room	99	2.56	2 [#23]	
13	55°C	14	1.08	2 [#25]	
14	55°C	14	2.56	2 [#23]	
15	55°C	99	1.08	2 [#25]	
16	55°C	99	2.56	2 [#23]	

The third factor (factor C) was the dopant weight percentage due to its known direct correlation to the helical shape of the CLC, which enables the Bragg grating phenomenon described in Section 2.1. The two levels were the upper and lower boundaries as discussed in Subsection 3.1.2: 1.08% and 2.56% weight dopant. Only two dopant levels were chosen to keep the design of the experiment balanced such that each factor contained the same amount of levels. This is the most efficient use of the statistical method, resources, and

33

time such that the number of experimental runs were minimized. More levels would increase the number of total runs, which means more time and resources spent, resulting in a negligible improvement of statistical data [52].

The experiment was planned to be conducted twice to account for LC cell defects as a nuisance factor. The first batch, or replicate, used a different pair of LC cells than the second replicate. For reference, the first replicate used cell identification numbers 15 and 17. The second used Cell ID numbers 23 and 25 according to the table above. These decisions resulted in two temperatures, two pressures, and two dopant concentrations which yielded eight experimental runs that accounted for all combinations of these factors and levels. The two replicate experiments, each with eight LC cells, brought the total to 16 run combinations that completed the overall experiment as seen in Table 4.

3.2.2. Experimental Process

Since LC cells were reused, there was not a CLC preparation phase. As a result, there was only one phase, spectral measurements. The equipment from the previous experiment (Subsection 3.1.3) was used with the exception of the light source. A broadband halogen lamp with a fiber couple was used in order to obtain a greater light source intensity. The light emitting diode lamp was not sufficient for this experiment due light dispersion created by the extra distance the input light needed to travel as seen in Fig. 14. A vacuum chamber was implemented to control the level settings for the pressure.

The commercially purchased vacuum chamber was a 2.75-quart clear rectangular pyrex glass container. Inner dimensions of the top of this container were 9.125 in long by 7.25 in wide. The height was 2.875 in tall with side walls that tapered to a smaller base at

8 in long by 6 in wide. The thickness of the pyrex glass was approximately 0.25 in on any face. The container was covered by a 0.75-in thick clear acrylic lid with a neoprene seal adhered to the bottom. A pressure regulator and two inlet/outlet valves were preinstalled on the lid. A hotplate, thermocouple, and multimeter were used to control the levels settings of the temperature during measurement. The vacuum chamber was able to maintain a seal with the thermocouple wire protruding out between the neoprene seal and the pyrex glass container. Spare pieces of neoprene and rubber were used to supplement the existing seal if any leaks occurred. A photograph of the test bench is found in Fig. 14 below.
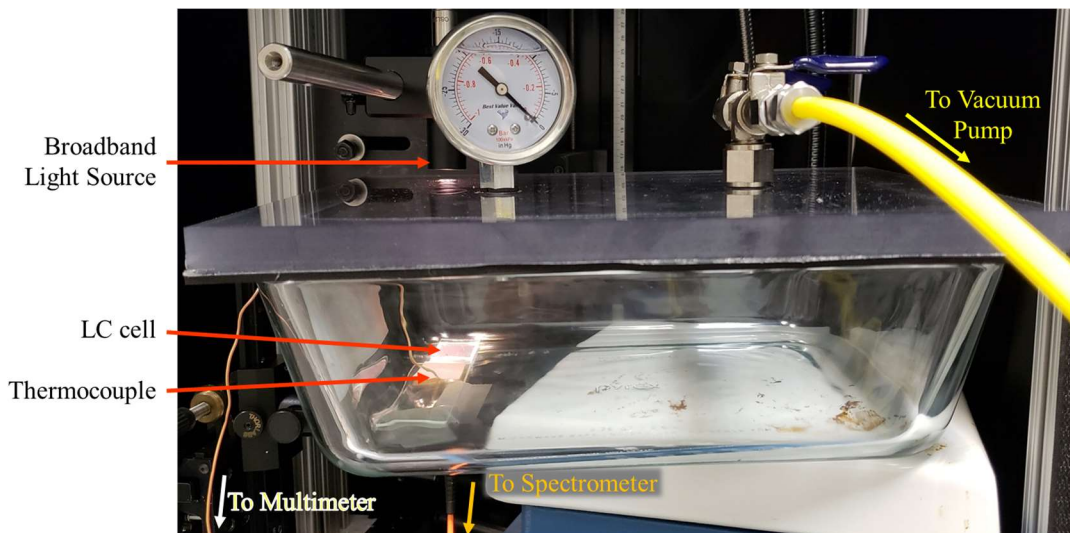
Figure 14. Configuration of equipment for the three-factor experiment.

An experimental run (a single row on Table 4) started with placing the appropriate LC cell in the vacuum chamber, and the lid was seated on top. If the run required a 55°C temperature level, then the temperature setting was adjusted on the hotplate until the target temperature in the vacuum chamber was reached. The hotplate was not turned on for room temperature. Afterward, if the run required a 14 kPa level, then the air in the vacuum

chamber was evacuated via an electric air compressor, and the valves were sealed. For a 99 kPa level, the air compressor was not used, and the vacuum chamber was left at the ground-level atmospheric pressure of the room. The valves were also sealed to not disperse heated air during measurement.

Next, the necessary background calibrations were conducted before the measurement of the LC cell. One measurement of an LC cell resulted in a percent transmission versus wavelength spectrum plot. Optical bandgap slopes were defined as percent transmission per wavelength (in nanometers). For each LC cell, three spectral measurements of that cell were captured in random locations. This accounted for variability in CLC alignment and dopant concentration across a single cell. Each spectrum was analyzed via a custom MATLAB algorithm (Appendix B) to find the steepest slope created by the edges of the optical transmission bandgap. This was done to create a consistent, repeatable process when analyzing the data to further eliminate variability between multiple experimenters. The three identified slopes were averaged together to obtain the final slope result for a single LC which was inputted into Table 4. An absolute value was used since the sign of the slope measurement is irrelevant to the slope's magnitude. This process was used for all 16 runs. The run order was randomized during the experiment to avoid errors that may affect the statistical analysis, such as, degradation of a piece of equipment or sample over time. The observation data was inputted into statistical software, Minitab 17, to calculate the ANOVA and determine the factors and interactions that were significant to changing the optical bandgap slope, which is found in Section 4.2.

www.manaraa.com

3.3. Theoretical Optoacoustic Detection Using LC

Research transitioned to the application of liquid crystal through optoacoustic detection. Subsection 3.3.1 describes the link between LC and OAD. Subsection 3.3.2 explains the steps of finding the LC OAD theoretical response to an acoustic stimulus.

3.3.1. *Liquid Crystal and Optoacoustic Detection*
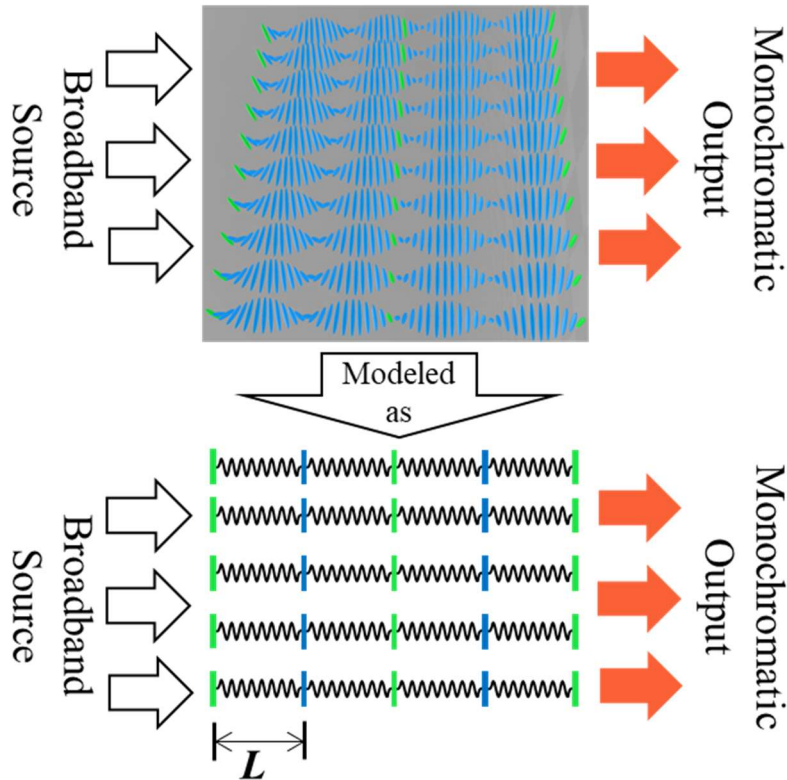
Figure 15. Schematic representation of thin-film CLC as arrays of periodic mirrors linked by molecular springs with half-pitch length, *L*.

Liquid crystalline materials undoubtedly represent a fascinating state of matter, combining liquid-like fluidity and crystal-like ordering. This soft, nonrigid property ideally makes LC responsive to various stimuli, such as acoustic pressures per Section 2.1. Current OADs are tested in liquid environments due to the improved acoustic transmission as

37

opposed to air (Section 2.2). The doped liquid crystal, or cholesteric LC, that align to form the spring-like, tunable Bragg grating are naturally responsive to external agitations. The spectral transition regime, or edge, in the optical transmission bandgap of the CLC grating can be used to sense broadband acoustic waves.

The resonant center wavelength (λ_0) of the thin-film CLC is given by

$$\lambda_0 = 2 \cdot L \cdot n_{Eff}, \tag{4}$$

where n_{Eff} and L are the effective refractive index and half-pitch length of the CLC grating respectively. As soundwaves impact the CLC, the optical mode in the CLC molecular grating undergoes a spectral shift due to the changes in n_{Eff} and L because of the photoelastic effect and physical deformation, respectively. This can be expressed as

$$\frac{\Delta\lambda}{\lambda_0} = \frac{\Delta n_{Eff}}{n_{Eff}} + \frac{\Delta L}{L}, \tag{5}$$

where $\Delta\lambda$, Δn_{Eff}, and ΔL are the change in wavelength, change in the effective refractive index, and the change in pitch length respectively. These equations were derived from references in Chapter II [10], [39]. The change, or modulation, in transmission intensity due to the shift in wavelength can be detected most at the falling or rising edge of the bandgap. A light source with a narrow wavelength can be matched, or locked, to this edge.

This is achieved by filtering a broad-spectrum white light with a narrow optical bandpass filter or via a laser light source. This enables recording of the time-domain modulation of transmission intensity at the falling or rising edge of the transmission bandgap. Ultimately, the analog acoustic vibration was detected using the transmitted optical properties of CLC resulting in liquid crystalline optoacoustic detection. In theory,

38

the sensitivity of this LC OAD increases with slope of the optical transmission bandgap edge. As a result, a small shift in the bandgap's center wavelength results in a large change in output light intensity, or percent transmission. The sensor does not need external amplifiers due to this inherent ability of the CLC to improve performance with the slope of the bandgap edge.

3.3.2. Characterization of the Theoretical LC OAD Response

Similar to Sections 3.1 and 0, the characterization of the theoretical LC OAD response began with measuring the optical transmission bandgap of the thin-film CLC, which was identified using the measurement setup described in Fig. 16. (a). Per Subsection 3.1.3, liquid crystal cells were previously prepared with different dopant concentrations of 4-Cyano-4'-pentylbiphenyl and chiral dopant R5011 as shown in Fig. 16. (b). The optical transmission bandgap from LC Cell #16 (2.05% weight dopant) was chosen for this theoretical computation based on the results found in Section 4.1.

Next, the calculations assumed a similar setup to that of Fig. 17 (b). The key mechanism to the LC OAD was creating a narrow-bandwidth of light that aligned with the wavelength at either the falling or rising edge of the transmission bandgap as depicted in Fig. 17. (a). To accomplish this, an LED white light source and optical filter was used instead of a laser to drive the LC cell. A broadband source is generally more affordable, compact, and practical than a bulky, expensive laser. The broadband light was filtered using a laser line, or narrow optical bandpass, filter, in which the center wavelength was 632 nm with a 1-nm FWHM (full-width at half-max). As the CLC deforms and the transmission bandgap shifts, the laser line filter only transmits a single wavelength that

39

changes light intensity over time. The intensity of the light transmitting through the LC cell and laser line filter was converted to an electrical signal via a photodetector (New Focus Model 1601).
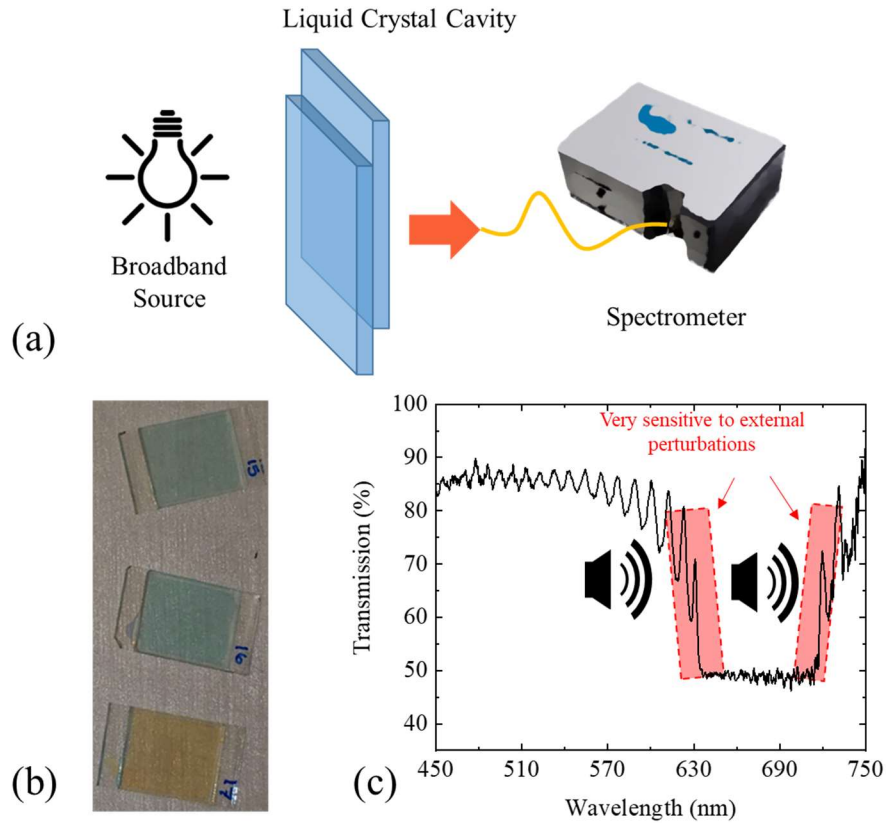
Figure 16. Experimental diagrams and samples: (a) The measurement setup to identify the optical resonance of thin-film CLC. (b) CLC cells with 1.08% wt (#15), 2.05% wt (#16), and 2.56% wt (#17) of chiral dopant. (c) A sample spectrometer measurement of the CLC resonance. Transmission bandgap edges are highlighted.

As a reference detector, a commercially acquired acoustic sensor and the accompanying amplifier were calibrated to accurately convert the time-domain peak-to-peak voltage into peak-to-peak acoustic pressure. The manufacturer of this sensor was G.R.A.S. and the model number was 46BE. The reference detector was separately tested

40

to provide a real-word comparison to the theoretical LC OAD response. In practice, an LC cell and the reference detector were placed next to each other to experience the same acoustic pressures, which was experimentally implemented in Section 3.4. An amplified function generator in-line with an acoustic transducer emitted the acoustic waves. The test stand was situated on an anti-vibration optical table with the acoustic transducer on a separate, uncoupled support structure. A broad frequency range, which included infrasound to ultrasound, was launched from the acoustic transducer. The time-domain and frequency-domain electrical signal spectra of the G.R.A.S. detector was recorded via an Agilent Inifiniium MSO8104A oscilloscope (Section4.4, Fig. 23). The MATLAB code used to read the data from the oscilloscope is found in Appendix C. Measurements for the LC cell response via the photodetector were also attempted, which are also discussed in Section 4.3.

The following assumptions were considered when calculating the theoretical characterization of the LC OAD response. Per Section 2.1, the elastic property of the LC (specifically LC5CB) was estimated to be similar to that of water, while the LC viscosity (25 mPa·s) is roughly 25 times that of water [18]. Knowing that the mechanical effective stiffness constant of water is approximately 10 mN/m [19], it was theorized that the stiffness constant of LC (k_{eff}) is 25 times 10 mN/m, resulting in k_{eff} = 250 mN/m.

Pressure of an incident soundwave (P) was found through converting the peak-to-peak voltage of the G.R.A.S. sensor using the given equipment documentation. The reference detector is calibrated to output 4 mV peak-to-peak for every 1 Pa of air pressure exerted against the reference detector's surface area (A). The force of the pressure wave,

F, was found using the definition of pressure, $F = P * A$. Using the previous assumptions, the water properties were converted to theoretical LC properties with Hooke's law, $F = k_{eff} * \Delta L$. This resulted in the value for ΔL, the amount of distance the water droplet was theoretically displaced, or compressed, by the pressure wave.
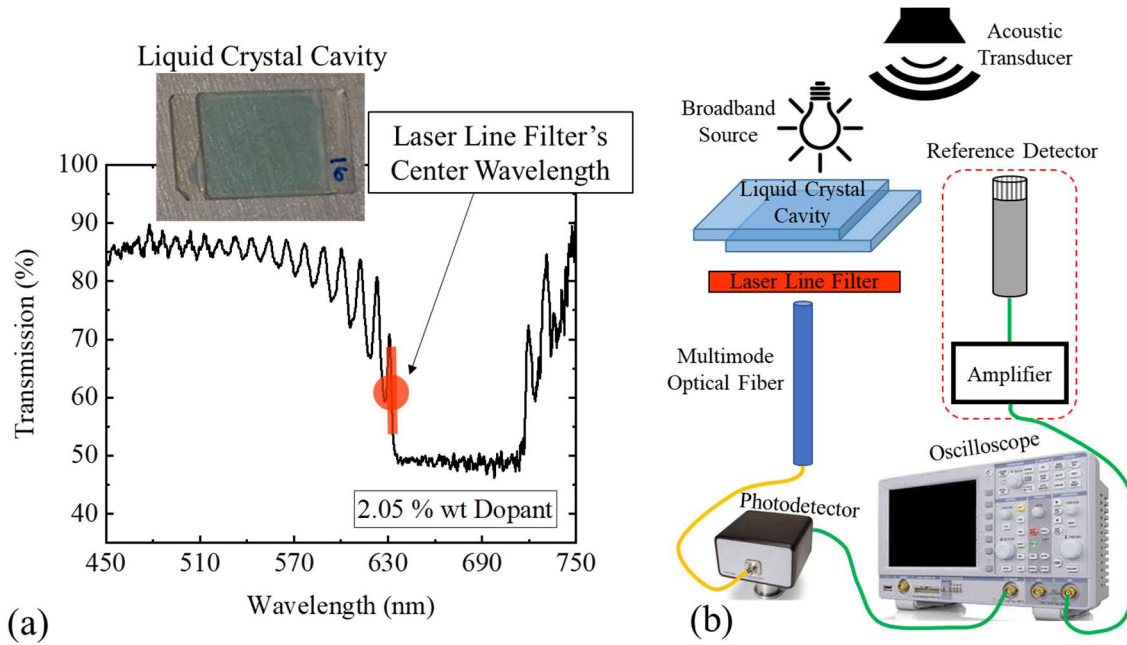
Figure 17. Filtering the broadband spectrum and experimental bench: (a) A laser line filter was used to produce a coherent input light at the most sensitive part of the LC transmission curve. (b) Schematic of the optoacoustic measurement test bench. A calibrated commercial acoustic sensor (G.R.A.S. 46BE with a preamplifier) designed for 4 Hz–100 kHz was used as a reference detector.

Equation (5), from the previous subsection, was used to describe the spectral wavelength shift ($\Delta\lambda$) observed due to the physical deformation of the LC. However, in this calculation, ΔL is as previously defined above, and L is the initial height of the water droplet in the research by Q. Ni et al [19]. Given a LC film thickness of L, it is assumed that the LC will deform by ΔL due to the acoustic pressure. The ratio of $\Delta L/L$ is then

42

proportional to any CLC thin-film thickness or pitch-length. The highly deformable LC was expected to dominate the change in wavelength compared to the photoelastic effect due to the helical pitch of the CLC directly corresponding to its transmitted optical spectrum (Section 2.1). As a result, the $\Delta n_{eff}/n_{eff}$ term was ignored, simplifying the equation to

$$\frac{\Delta\lambda}{\lambda} = \frac{\Delta L}{L}. \tag{6}$$

This was used to find $\Delta\lambda$ with the known values of λ (laser line filter wavelength), ΔL, and L.

The expected change in percent transmission ($\Delta T_{\%}$), or the light intensity, was found using the plot of the optical transmission bandgap, the calculated $\Delta\lambda$, and λ. The acoustic pressure compressed the CLC helical pitch and color-shifted the bandgap center wavelength to a lower wavelength, which was illustrated in Section 2.1, Fig. 3. Assuming that the plot retains its shape during an actual shift, the theorized shift was extrapolated from the measured plot of the optical transmission bandgap in Fig. 17 (a). A single point on the spectrum plot translated to a wavelength with a corresponding intensity, or percent transmission. $\Delta T_{\%}$ was calculated by finding the difference of percent transmission between the plot at λ and plot at $\lambda + \Delta\lambda$.

An initial photodetector voltage level (V_i) was required to plot the final LC OAD theoretical response as a voltage versus time plot. V_i was measured using the test configuration in Fig. 17 (b), in which the light source was transmitted through the LC cell and laser line filter and converted to a readable voltage level via the photodetector and

43

oscilloscope. V_i was then assumed to be the voltage level at the moment in time when the LC cell experienced least amount of pressure due to the soundwave. The final voltage level (V_f) was assumed to be voltage level at the moment when the LC cell experiences the most amount of pressure due to the soundwave, which was calculated by

$$V_f = V_i - (V_i * \Delta T_\%),\tag{7}$$

where $\Delta T_\%$ was previously found above. Using these results and the standard equation for a sine wave, the detected unamplified modulated light intensity was analytically calculated and plotted in the time-domain. This was also converted to the frequency domain via Fast Fourier Transform (FFT). The amplitude of the time-domain sine wave was $V_f - V_i$. This calculation was repeated for each of the frequencies tested (Section 4.3, Fig. 23).

3.4. Experimental LC-Enhanced Photophone

As an incremental design, the following optoacoustic detector using LC was created and tested with the acoustic source directly-coupled (in-contact with no air gap) to the device. This section is divided into LC cell manufacturing and preparation (Subsection 3.4.1) and the measurement of the response of an LC-enhanced photophone.

3.4.1. Photolithographed LC Cell

Research branched from the commercially bought LC cell to pursue a customized design due to the results from the experiment explained in Section 3.3 and 4.3. Manufacturing of a new LC cell began with a glass plate substrate with dimensions of 73 x 23 x 1 mm, a standard microscope slide. A 3.1 μm layer of SF 1818 photoresist was spun-onto the glass plate in accordance the process follower in Appendix D. A 5mm wide trench

was developed into the photoresist across the middle of the glass plate, width-wise. This resulted in a 5mm trench bordered by photoresist walls with a step-height of 3.1 μm.
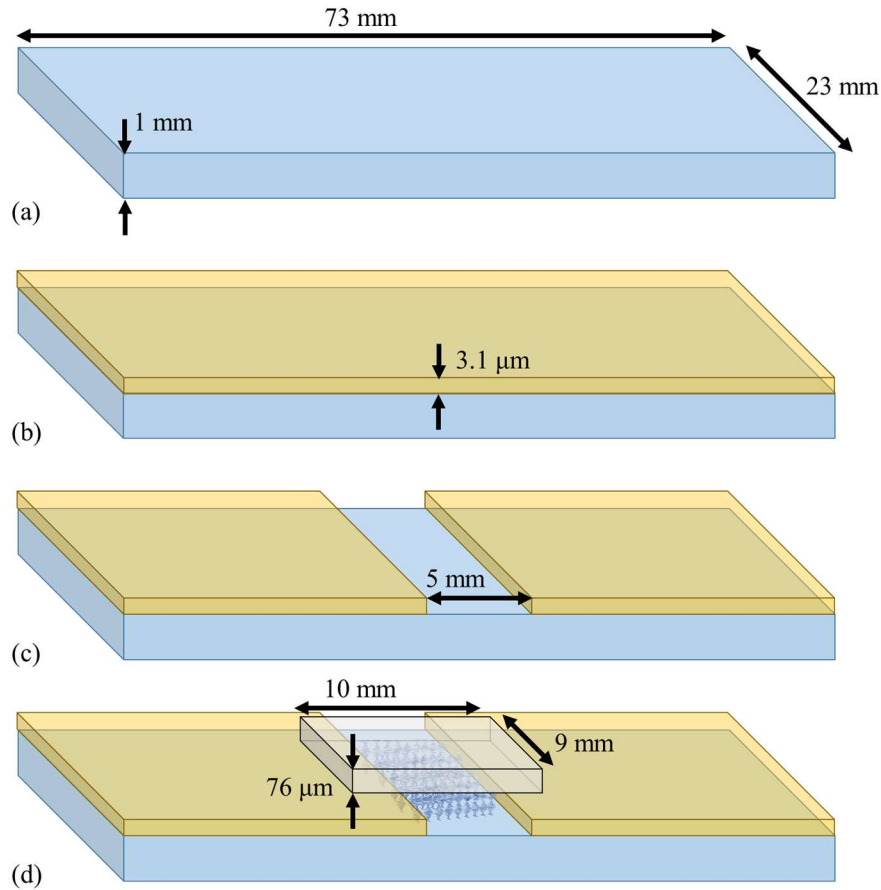
Figure 18. Construction of a customized photolithographed LC Cell. (a) The glass plate substrate. (b) SF 1818 photoresist deposited onto the substrate. (c) 3.1 μm trench created via photolithography. (d) CLC deposited into the trench with the polyethylene cover set on top. Image is not drawn to scale.

The step height was chosen to closely match the 3 μm gap of the commercial LC cell. This was created via photolithography using a process follower found in Appendix E. This completed the base of the LC cell. A clear plastic sheet of polyethylene with a thickness of 76 μm was used for the cover, which was cut into a 10 x 9 mm rectangular

45

piece. A step-by-step illustration is shown in Fig. 18 (a-c). The polyethylene was chosen to act as a flexible barrier between external pressures and the CLC as opposed to a rigid glass barrier found on the commercial glass LC cell.

Similar to the previous section, the CLC mixture with a concentration of 2.05% weight dopant was chosen for the device per the results in Section 4.1. The CLC was deposited into the trench of the photolithographed base. The polyethylene cover was placed over the deposited CLC to complete the finished, loaded LC cell as seen in Fig. 18 (d) and FigA spectral measurement of the loaded photolithographed LC cell's transmission bandgap is found in Section 4.4.

3.4.2. LC-Enhanced Photophone Measurement

To demonstrate the intrinsic enhancing nature of cholesteric liquid crystal, a simple photophone (Subsection 2.2.1) augmented by the chiral-doped LC was created. However, instead of a mirror, the photolithographed LC cell from the previous subsection above was used as the detecting medium. The new test bench was similar to that described in Subsection 3.3.2 and Fig. 17. (b), however, the following alterations were made. A halogen light source, as used in Subsection 3.2.2, was used to achieve a greater input intensity than the LED source. A 50x magnifying objective lens was placed between the light source and LC cell. This was oriented such that the light from the source was focused through the LC cell and into the fiber optic probe. This was added to further increase the light source intensity, a modification instigated by the results in Section 4.3.
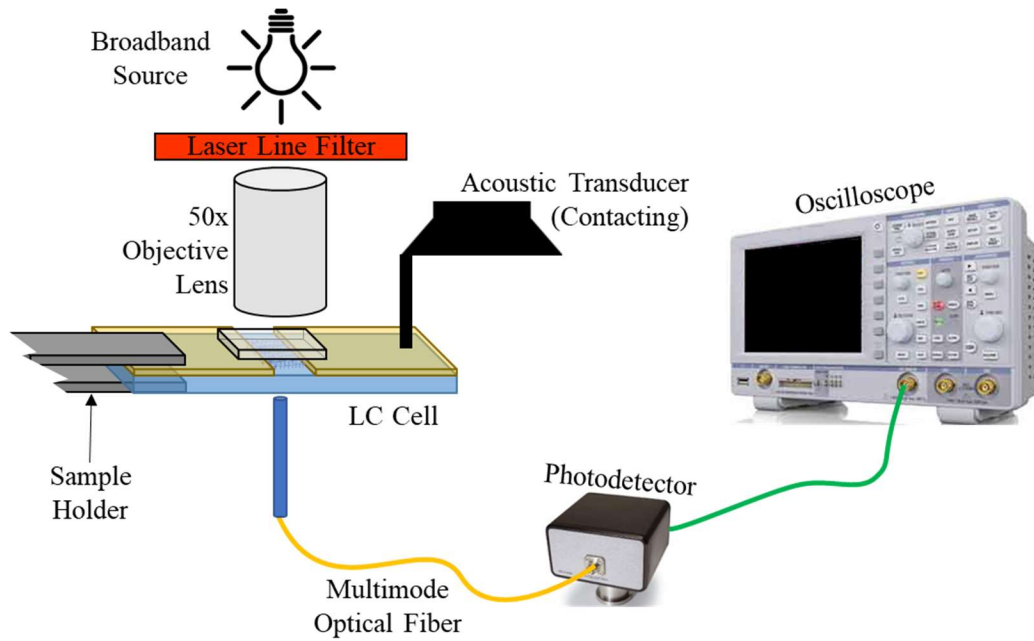
Figure 19. Schematic of the photophone measurement test bench. The photolithographed LC cell is pictured as the sample under test.

The laser line filter was moved to the space in between the light source and the 50x objective lens for ease of removing the filter for spectrometer calibration. The acoustic transducer was situated such that it physically contacted the LC cell or the reference detector. Contacting the LC cell or reference detector was spatially difficult due to the size of the acoustic transducer. A metal armature was connected to the acoustic transducer, which was able to contact the LC cell or reference detector in the confined space. As a result, simultaneous measurements of the LC cell and reference detector could not be achieved. A diagram of the complete setup is found in Fig. 19 above.
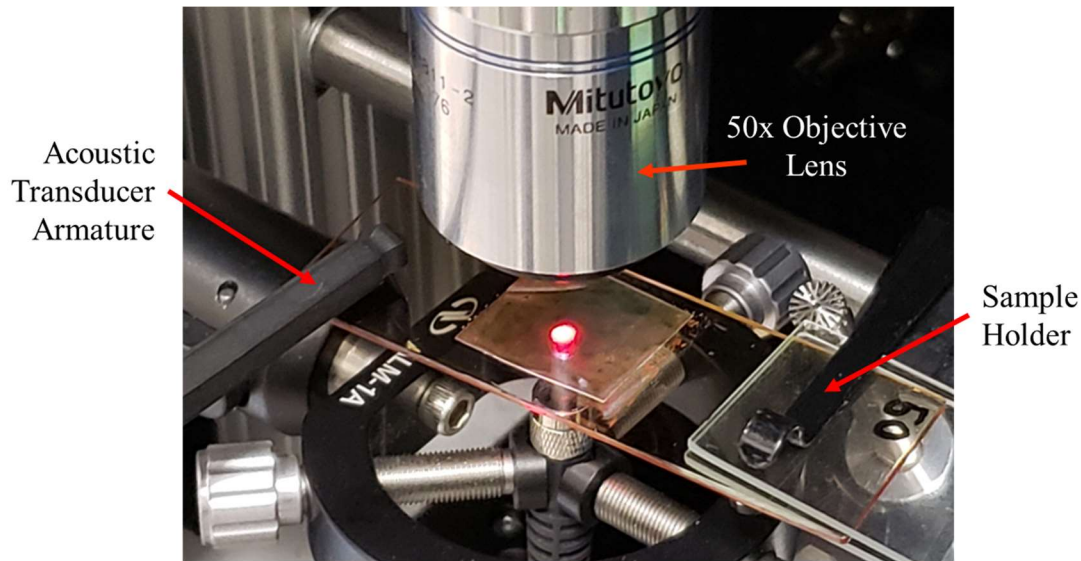
Figure 20. Configuration of LC-enhanced photophone experiment. The sample under test is the photolithographed LC cell loaded with CLC (2.05% wt dopant).

The new LC cell acoustic response was measured against both an unaltered glass plate (73 x 23 x 1 mm) and the reference detector. Measurement began with placing the new LC cell sample into the holder with a 5 cm overhang. The acoustic transducer armature was contacted to the LC cell at 1 cm from the end of the sample as seen in Fig. 20. The placement of the LC cell and the acoustic transducer armature was important to create similar mechanical conditions of the photophone when comparing results with the unaltered glass slide. A 60 Hz acoustic signal was launched through the acoustic transducer armature, and photodetector time-domain measurements were captured via the oscilloscope, which is displayed in Section 4.4, Fig. 26-28. This was repeated for measurement of the unaltered glass plate photophone and the reference detector. For the reference detector, placement of the acoustic transistor armature was directly on the sense-end of the detector.

48

3.5. Summary

The four sections previously described were a series of sequential research efforts that used fairly similar equipment, but largely different methods to study the responses of Cholesteric Liquid Crystal. Section 3.1 described the Analysis of Variance statistical experiment to find the significant sources of variation, or factors, to the transmission bandgap slope. These sources were based on the way CLC was prepared: the loading temperature of the LC cell, the dopant concentration, and the interaction between those two main factors. Section 3.2 used the same ANOVA method but had three main factors and their interactions as the sources of variation. The dopant concentration factor was carried over from the previous experiment, but two of those main factors focused on environmental variables: pressure and temperature around the LC cell at the time of spectral measurement.

Section 3.3 detailed how the measured response of a commercial audio detector was used to calculated the theoretical optoacoustic response of a thin-film CLC. The crucial physical property was how incident acoustic pressure waves cause the pitch of the CLC to physically deform, thus, creating a shift of the CLC's optical transmission bandgap. Section 3.4 explained how to create a custom LC cell through photolithography. Subsequently, research concluded with constructing an LC-enhanced photophone to demonstrate the optoacoustic enhancing abilities of cholesteric liquid crystal.

www.manaraa.com

IV. Analysis and Results

Chapter IV interprets the results of the efforts pursued in Chapter III. Section 4.1 contains two-factor statistical table results from Section 3.1. The three-factor statistical tables are found in Section 4.2, which correspond to the method in Section 3.2. The theoretical LC OAD plots (Section 4.3) from the preceding calculations (Section 3.3) are also presented. Lastly, Section 4.4 displays the time-domain oscilloscope readings from the experiment in described in Section 3.4.

4.1. Two-Factor Statistical Design Experiment

Table 5. Observed measurements of the two-factor analysis with replication. Each observed measurement, absolute value of average slope, was calculated from three random measurements from the same LC cell.

Run	Cell ID #	Loading Temperature	Dopant (%wt)	Replicate #	|Avg. Slope| (%trans. / nm)
1	14	Room	0	1	0.9042
2	15	Room	1.08	1	3.2463
3	16	Room	2.05	1	3.9377
4	17	Room	2.56	1	3.4337
5	18	103.9°C	0	1	0.8870
6	19	103.9°C	1.08	1	4.0762
7	20	103.9°C	2.05	1	4.7139
8	21	103.9°C	2.56	1	3.0628
9	22	Room	0	2	0.7142
10	23	Room	1.08	2	3.2219
11	24	Room	2.05	2	3.8401
12	25	Room	2.56	2	2.5776
13	26	103.9°C	0	2	0.6528
14	27	103.9°C	1.08	2	2.2744
15	28	103.9°C	2.05	2	2.6642
16	29	103.9°C	2.56	2	3.0335

This section includes the results from the experiment in Section 3.1. The first batch of data was the individual slope measurements of each LC cell. Per Subsection 3.1.3, three absolute value slope measurements were taken from each of the 16 LC cells. A full list of the 48 individual measurements is found in Appendix F. For each LC cell, those three measurements were averaged and recorded (Table 5). These 16 averaged measurements were inputted into statistical software, Minitab 17, to evaluate the ANOVA calculation, in which the output is displayed in Table 6 with evaluated p-values in Table 7.

Table 6. ANOVA table calculated from the equations in Table 3. P-value evaluations are on table found on Table 7.

Source of Variation	Sum of Squares	Degrees of Freedom	Mean Square	F_0
Factor A (Loading Temp.)	0.0163	1	0.0163	0.03
Factor B (% wt Dopant)	20.7887	3	6.9296	13.39
Interaction (A & B)	0.0304	3	0.0101	0.02
Error	4.1413	8	0.5177	
Total	24.9768	15		

The ANOVA algorithm resulted with only one factor that significantly affected the slope of the optical bandgap edge under a p-value of 0.05: the dopant concentration as seen on Table 7. This analysis also indicated that the loading temperature and the interaction between loading temperature and dopant concentration are not significant. Consequently, the loading temperature of an LC cell would not be accounted for in a future design.

51

Table 7. Summary of two-factor ANOVA output calculated with only two factors and one interaction, showing factor B as significant due to p-value < 0.05.

Variation Source	P-Value
Main Factor A: Loading Temperature	0.863
Main Factor B: Dopant Concentration	**0.002**
Interaction Between A & B	0.996

As explained in Subsection 3.1.2, the ANOVA was recalculated while including the nuisance factor, LC Cell defects, or replicates, as a source of variation. Significant and insignificant factors and interactions remained unchanged as seen on Table 8. The nuisance factor was very close to significantly affecting the slope due to a p-value of 0.059, which means that more testing is necessary to evaluate its significance level. This source of variation may require more experimental runs and better accounting of where and when an empty LC cell was manufactured to better determine the factor's significance.

Table 8. Summary of two-factor ANOVA output with LC cell defects (replicates) included as a source of variation, showing factor B as still significant due to p-value < 0.05. LC cell defects was inconclusive since the p-value is close to the 0.05 threshold.

Variation Source	P-Value
A: Loading Temperature	0.833
B: Dopant Concentration	**0.001**
Interaction Between A & B	0.993
LC Cell Defects (Variation Between Replicates)	*0.059*

Additionally, the 2.05% weight dopant mixture was empirically found to yield the greatest, or steepest, average slope as seen in Fig. 21. Using these conclusions, a sensor

52

that depends on a steep optical bandgap slope can be optimized using the 2.05% weight dopant mixture. This dopant concentration was implemented in the theoretical and experimental LC OAD sections, Section 3.3 and 3.4 respectively.
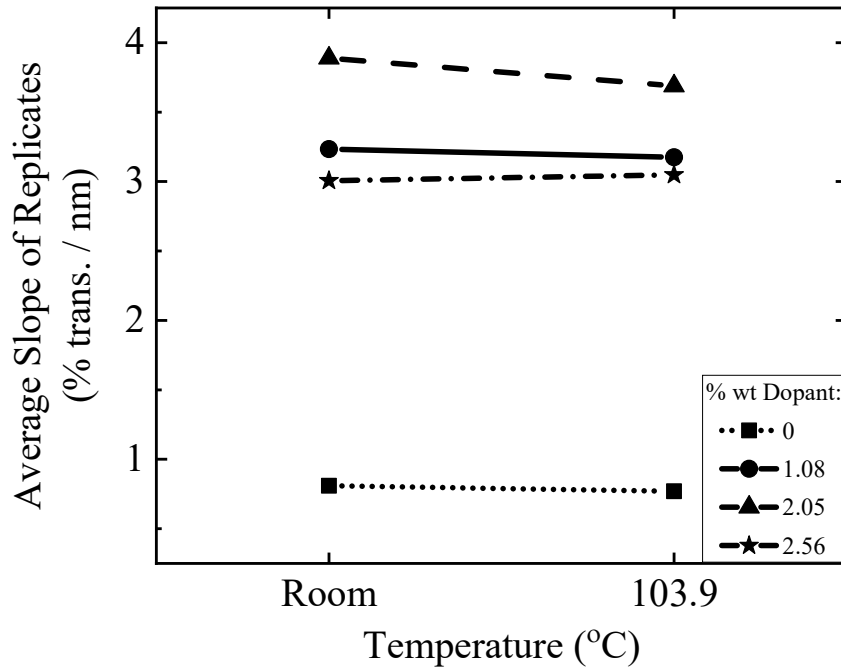
Figure 21. Plotted trends for average slope of replicates versus loading temperature levels. Each point is an average slope of both replicate values. For example, the average slope of cell # 14 and # 22 is the single bottom-left point of the plot.

This fact, however, was limited to the specific materials that were used in this study, such that, a similar mixture in a different LC cell may not yield the same results. This results from the ringing effect, or interference fringes, due to thin-film interference of the gap between LC cell glass plates, which is similar to the optical phenomena of the etalon OAD (Subsection 2.2.1). It was apparent that all the spectrum measurements above (e.g. Fig. 11) appeared to have this high frequency, sinusoidal-like waveform throughout the

53

figure. These interference fringes coupled with the CLC optical bandgap interact such that the interference fringes contribute to the steepest bandgap slope for any given CLC mixture. However, this would suggest that special attention is required during the construction of the LC cell cavity especially when choosing the glass thickness and gap spacing. This was taken into consideration in when preparing the custom LC cell in Subsection 3.4.1. Conclusions and recommendations for this section are found in Section 5.1.

4.2. Three-Factor Statistical Design Experiment

Table 9. Observed measurements of the three-factor analysis with replication. Each observed measurement, absolute value of average slope, was calculated from three random measurements from that same LC cell.

Run	Factor A: Measurement Temperature	Factor B: Pressure (kPa)	Factor B: Dopant (%wt)	Replicate # (Batch) [Cell ID #]	Observation: |Avg. Slope| (%trans. / nm)
1	55°C	14	2.56	1 [#17]	4.4021
2	55°C	14	1.08	1 [#15]	4.1792
3	55°C	99	2.56	1 [#17]	5.6918
4	55°C	99	1.08	1 [#15]	5.1215
5	Room	14	2.56	1 [#17]	5.0559
6	Room	14	1.08	1 [#15]	6.6638
7	Room	99	2.56	1 [#17]	4.9264
8	Room	99	1.08	1 [#15]	5.7432
9	55°C	14	2.56	2 [#25]	4.2579
10	55°C	14	1.08	2 [#23]	5.3585
11	55°C	99	2.56	2 [#25]	4.8934
12	55°C	99	1.08	2 [#23]	4.6122
13	Room	14	2.56	2 [#25]	4.5601
14	Room	14	1.08	2 [#23]	5.6570
15	Room	99	2.56	2 [#25]	5.0013
16	Room	99	1.08	2 [#23]	6.2295

This section includes the results from the experiment in Section 3.2. Similar to the previous section, the 16 averaged slopes are presented on Table 9 above. A full list of the 48 individual measurements is found in Appendix G. These 16 averaged measurements were inputted into Minitab 17 to evaluate the ANOVA calculation, in which evaluated p-value output is found in Table 10.

Table 10. Summary of three-factor ANOVA output calculated with three main factors and four interaction sources of variation. The interaction of main factors A and C was significant due to p-value < 0.05. The individual main factors A and C cannot be separately labeled as significant due to the masking effect of the higher order, significant interaction of A & C.

Variation Source	P-Value
A: Measurement Temperature	0.026
B: Pressure	0.317
C: Dopant Concentration	0.040
Interaction of main factors: - A (Measurement Temperature) - B (Pressure)	0.301
Interaction of main factors: - A (Measurement Temperature) - C (Dopant Concentration)	**0.042**
Interaction of main factors: - B (Pressure) - C (Dopant Concentration)	0.256
Interaction of main factors - A (Measurement Temperature) - B (Pressure) - C (Dopant Concentration)	0.599

The ANOVA algorithm indicated that an interaction between measuring temperature and dopant concentration significantly affected the slope of the optical bandgap edge with a p-value under 0.05 (Table 10). The individual main factors of

55

measuring temperature and dopant concentration cannot be separately labeled as significant due to the masking effect of the higher-order, significant interaction of measuring temperature and dopant concentration, as explained in Section 3.1.4. All other sources of variation were labeled as not significant to the variation of the slop of the optical transmission bandgap edge.

Table 11. Summary of three-factor ANOVA output with LC cell defects (replicates) included as a source of variation. LC cell defects is not significant due to the p-value > 0.05. Only factor A is labeled significant, however, factor C and the interaction of A & C are close to significant p-values, requiring further investigation. LC defects is not significant, which supports the previous ANOVA calculation.

Variation Source	P-Value
A: Measurement Temperature	**0.035**
B: Pressure	0.340
C: Dopant Concentration	*0.051*
Interaction of main factors: - A (Measurement Temperature) - B (Pressure)	0.324
Interaction of main factors: - A (Measurement Temperature) - C (Dopant Concentration)	*0.053*
Interaction of main factors: - B (Pressure) - C (Dopant Concentration)	0.279
Interaction of main factors - A (Measurement Temperature) - B (Pressure) - C (Dopant Concentration)	0.616
LC Cell Defects (Variation Between Replicates)	*__0.570__*

As explained in Section 3.2.1, the ANOVA was recalculated while including the nuisance factor, LC Cell defects, or replicates, as a source of variation (Table 11). LC cell defects was labeled as not significant due to a p-value of 0.570. The addition of the nuisance factor shifted three sources of variation above the 0.05 threshold: measurement temperature, dopant concentration, and the interaction between those two main factors. If the ANOVA output in Table 11 was analyzed by itself, those sources of variation would require more investigation to be labeled significant or not significant. However, since the variation due to replicates (LC cell defects) is not significant, the replicate experiment was able to be added to the overall pool of data. This improved the evidence from ANOVA calculation to reduce the p-value to below 0.05 per the previous analysis. As a result, the analysis from Table 10 was supported by the results in Table 11.

Ideal factor levels of the significant factors were empirically found through analysis of the 16 average slope values. For measurement temperature, the slope was the maximized when the measurement temperature was low (room temperature). For dopant concentration, the slope was maximized when the dopant percentage was low (1.80% wt dopant). The combination of the low measuring temperature and low dopant concentration resulted in the greatest mean of the average slopes. According to the bounds of this experiment, a sensor that depends on a steep optical bandgap slope is optimized when constructed with a 1.80% weight dopant concentration and operated at room temperature. The 1.80% weight dopant concentration was not used in either experiment due to the results from Section 4.1. The 2.05% weight dopant concentration did return the highest slope in the two-factor experiment, which means that there is a non-linear relationship between

slope and dopant concentration. As a result, the ouput data from this experiment requires further refinement, and only represents a proof-of-concept for future factors. Conclusions and recommendations for this section are found in Section 5.1.

4.3. Theoretical Response of the LC OAD

These results include the voltage versus time response plot of the experimental of the G.R.A.S. reference detector and the theoretical LC OAD from Section 3.3. Measured values of the CLC spectrum and photodetector are also presented. The three frequencies launched from the acoustic transducer source were 15 Hz, 14 kHz, and 50 kHz, which covered the infrasound to ultrasound range.
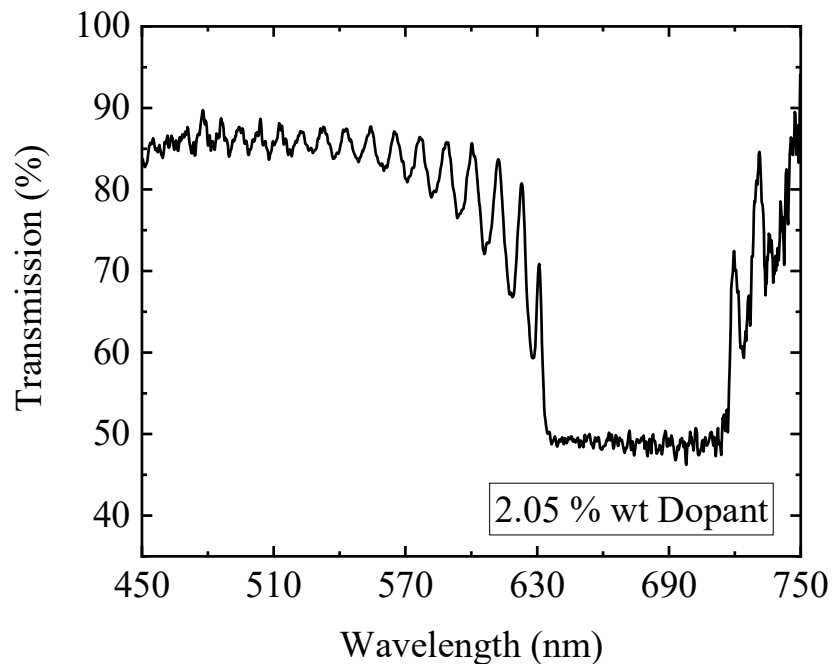
Figure 22. The measured optical resonance of the CLC with 2.05% wt dopant (Cell ID #16).

The measured center wavelength and slope of the transmission bandgap, or optical resonance, were approximately 675 nm and 5.9%/nm, respectively from Fig. 22. The initial

58

photodetector voltage level, V_i per Equation (7), was measured at 1.2 mV. This was the light intensity of the source light after it passed through the laser line filter and the CLC when the acoustic transducer was not on. The reference detector time-domain responses are on Fig. 23 (a, c, e), and the theoretical LC OAD responses are on Fig. 23 (b, d, f). An inset within the figures show the frequency versus time plots. Both were centered on 0 mV (AC-coupled) to easily compare peak-to-peak voltages. The resulting G.R.A.S sensor voltages are greater than those of the LC cavity ranging from 13, 47, and 14 times greater at 15 Hz, 14 kHz, and 50 kHz, respectively.

Although the transducer was found to be more responsive, the calculation indicated a higher intensity of light as the ideal method to increasing LC OAD sensitivity. The 1.2 mV detected intensity of the filtered white light source may not have enough intensity to yield a detectable optoacoustic signal. Ideally, a light source with an intensity measurement greater than (16 mV to 56 mV) 4 to 8 times that of the G.R.A.S peak-to-peak voltage will yield a more sensitive LC cavity acoustic detector depending on frequency. This discovery was carried forward to the light source decision in Subsection 3.4.2.

The intensity of this light source was compared to modern laser sources by calculating the power of the light as seen by the photodetector. The New Focus Model 1601 photodetector has a current gain of 700 V/A. A photodetector current was found by dividing the measured 1.2 mV level by the current gain, which resulted in 1.7 μA. Per the photodetector documentation, at the 600 nm wavelength peak response is 0.4 A/W. Dividing the photodetector current (1.7 μA) by this peak response (0.4 A/W) equals the power of the light source after it exits the LC cell and filter, which is 4.3 μW. In

comparison, the lowest level of laser classification, class 1, has approximately 1-30 mW of power.

Measurement of the time-domain response from the LC OAD (LC cell #16; 2.05% wt dopant) was attempted during the measurement of the reference detector. However, there was no discernable acoustic signal viewed in the oscilloscope. Per Fig. 23, theoretical the amplitude of the signal is at most 0.26 mV at 14kHz. As a result, it is possible that the experimental time-domain response of the LC OAD is too small and unreadable due to electrical noise. That is to say that the intended signal is below the noise floor. Further conclusions and recommendations are discussed in Section 5.2.
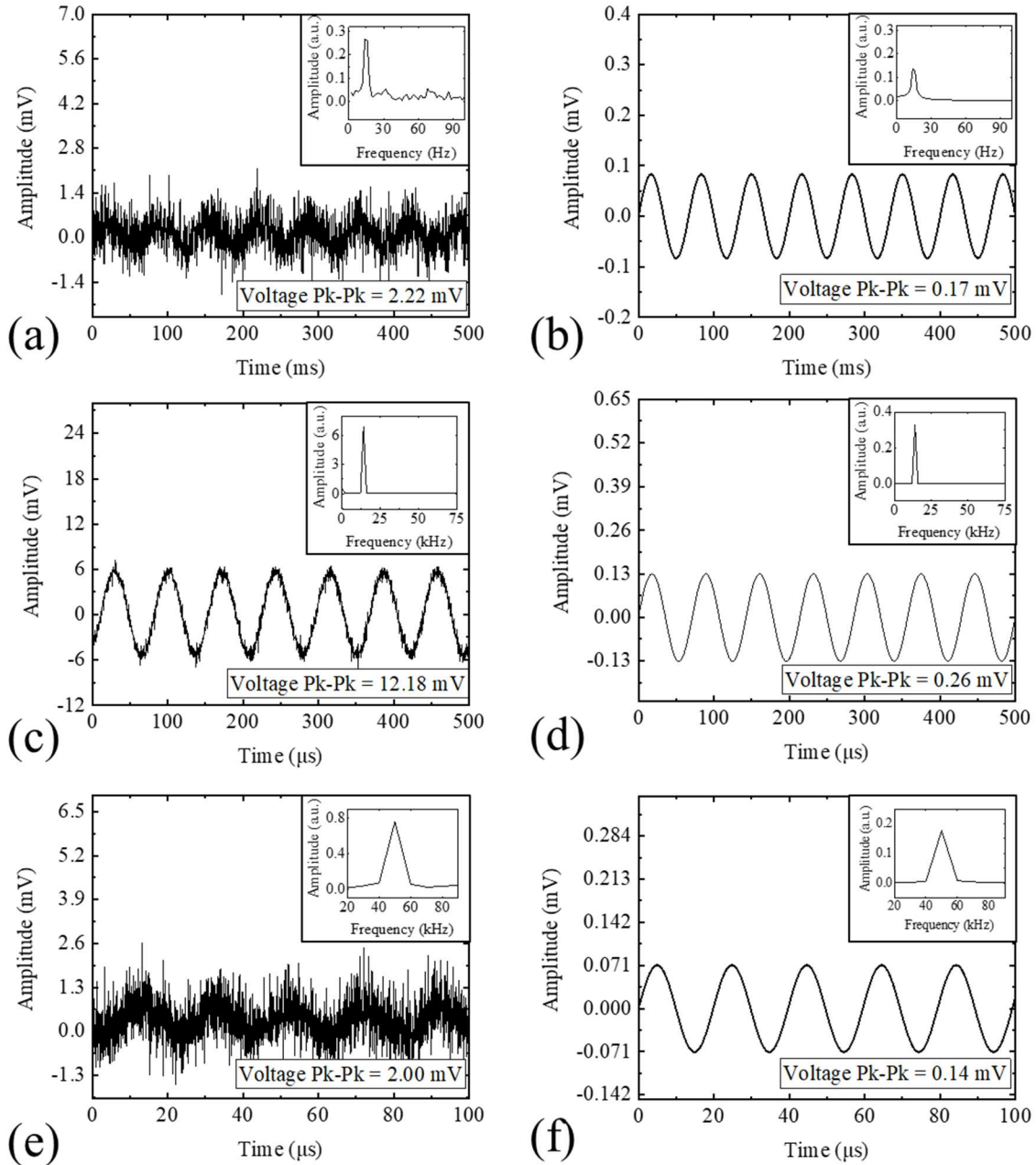
Figure 23. Temporal spectra of acoustic waves at (a, b) 15 Hz, (c, d) 14 kHz, and (e, f) 50 kHz detected by the reference sensor G.R.A.S. 46BE (a, c, e). The corresponding peak-to-peak pressures detected by the reference sensor were 0.56, 3.05, and 0.50 Pa respectively. The analytically estimated temporal spectra was found for the LC Cell (b, d, f).

4.4. Experimental LC-Enhanced Photophone

Results from this section correspond to the experiments described in Section 3.4. The initial results were from the spectrometer measurement of the unaltered glass plate and the CLC deposited on the photolithographed LC cell. As shown in Fig. 24, the unaltered glass plate did not have an optical transmission bandgap. As a result, there was no amplification of the output modulated light intensity due to a transmission bandgap edge. The slope near 623 nm, the wavelength of the laser line filter, was manually found to be 0.1 %/nm.
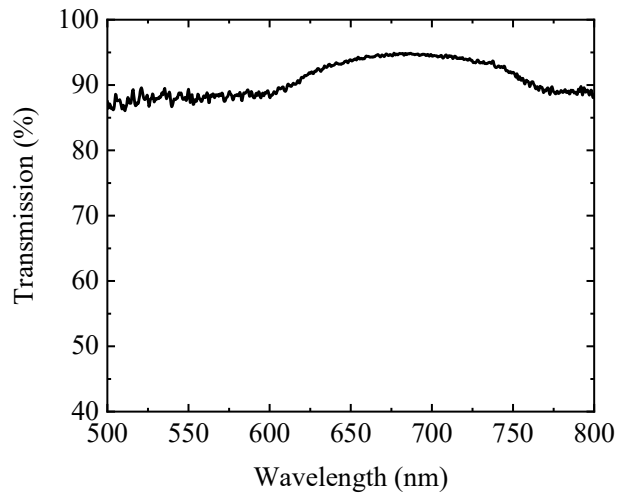
Figure 24. Measured optical transmission of unaltered glass plate.

In Fig. Figure 25, the custom LC cell (loaded with CLC), had a transmission bandgap. The slope near 623 nm was manually found as 1.3 %/nm, which is 4.3 times that of the untreated glass plate. Also, there was no sinusoidal ringing due to thin film interference as compared to Fig. 22. This was due to the gap step-height of the custom LC cell being larger than that of the gap between the glass plates in the commercial LC cell.

Previously measured commercial LC cell spectra had this ringing characteristic as seen in Fig. 22.
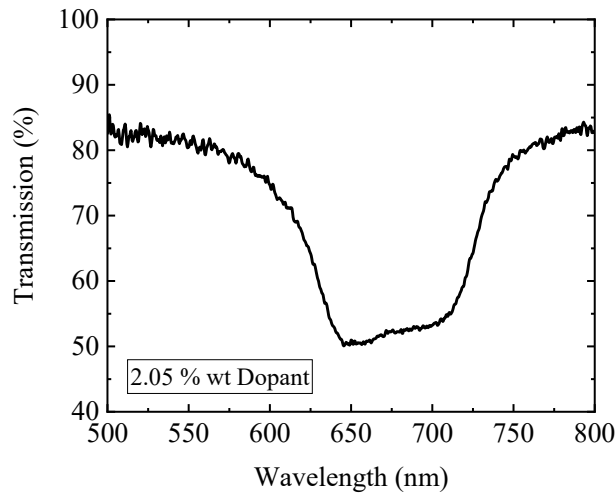
Figure 25. Measured optical resonance of the photolithographed LC cell loaded with 2.05% wt dopant CLC. The acoustic source was 60 Hz and contact-coupled.

The final results included temporal (voltage versus time) plots of the reference detector, unaltered glass plate photophone, and LC-enhanced photophone. Each device was tested with a 60 Hz, contact-coupled audio transducer. Each plot displays the time-domain response and contains an inset frequency-domain response, which was calculated via Fast Fourier Transform (FFT) using the original time-domain data (in black). Red plots were an average of 16 separate time-domain samples. The oscilloscope sampled at a rate of 3000 samples per second.

As a reference, the G.R.A.S. detector with its in-line amplifier returned an average peak-to-peak amplitude of 4.47 mV (Fig. 26). The unaltered glass plate photophone resulted in an average peak-to-peak amplitude of 0.34 mV without any external electrical amplification. The LC enhanced photophone produced a 0.53 mV peak-to-peak amplitude

63

when detecting the contact-coupled 60 Hz acoustic vibration. Although the reference detector amplifier provided no gain, it is worth noting that the detector is a refined commercial device that was designed specifically for these ranges of acoustic frequencies (4 Hz–100 kHz). The LC enhanced photophone was not electrically amplified, and produced a peak-to-peak voltage 1.6 times greater the amplitude of the untreated glass photophone. Conclusions and recommendations for this section are found in Section 5.2.
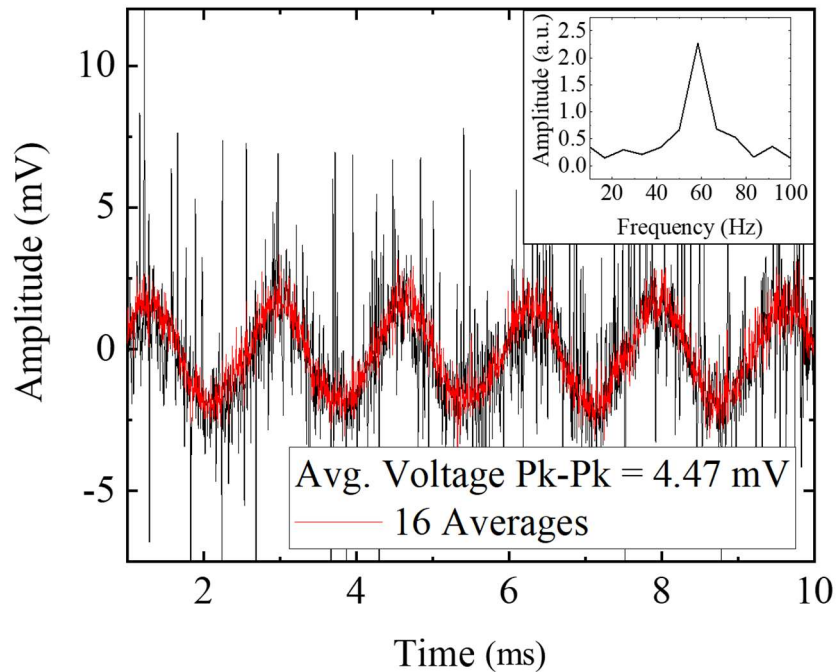
Figure 26. Measured temporal spectra of the reference detector. The acoustic source was 60 Hz and contact-coupled. The frequency-domain inset is an FFT of the original waveform in black.

64
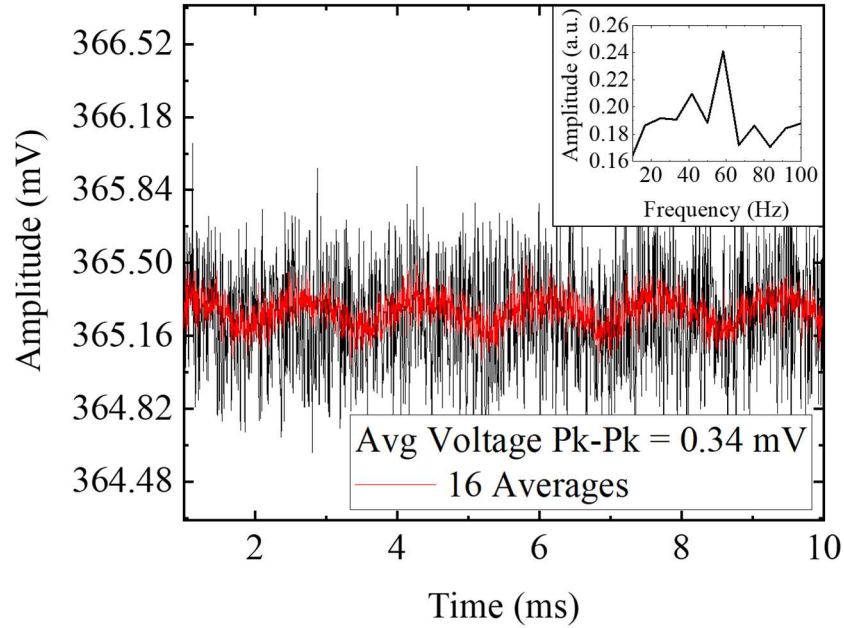
Figure 27. Measured temporal spectra of the photophone with unaltered glass plate. The acoustic source was 60 Hz and contact-coupled. The frequency-domain inset is an FFT of the original waveform in black.
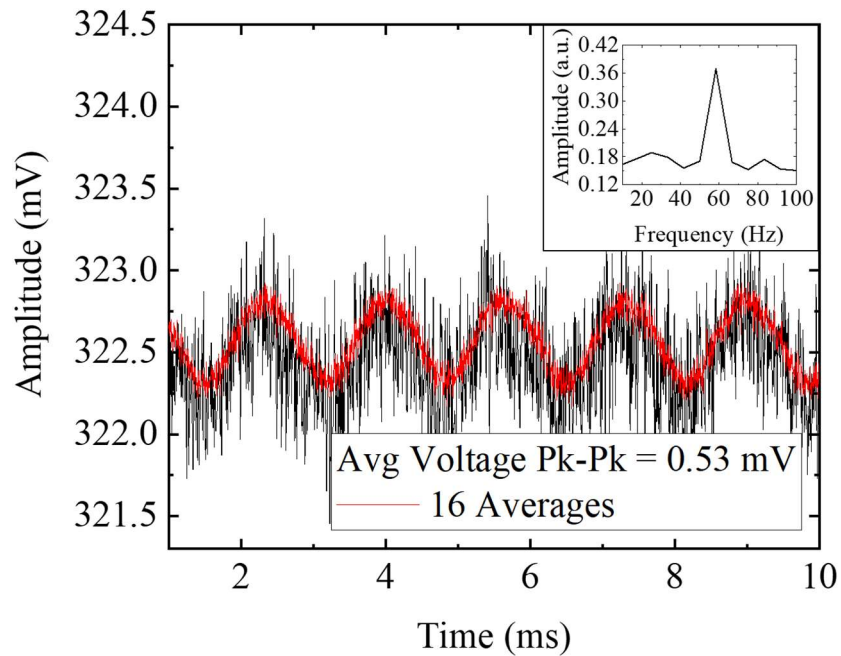
Figure 28. Measured temporal spectra of the LC-enhanced photophone. The acoustic source was 60 Hz and contact-coupled. The frequency-domain inset is an FFT of the original waveform in black.

65

4.5. Summary

The four sections previously described were a series of results from sequential experiments, each building upon its predecessor. The two-factor statistical design experiment in Section 4.1 verified that dopant concentration is the leading factor to bandgap creation, and that 2.05% wt dopant was the best candidate for optoacoustic detection due to maximizing transmission bandgap slope performance. Section 4.2, three-factor statistical design experiment, revealed that dopant concentration and temperature interact to significantly affect the slope. In addition, measuring at room temperature and using a lower dopant concentration were ideal to maximize the slope, in which the latter supported the two-factor statistical result. The LC cell cavity gap was also theorized to affect the optical transmission characteristics of CLC.

In Section 4.3 (theoretical response of the LC OAD), a CLC sample with 2.05% wt dopant concentration per Section 4.3. The theoretical acoustic response of the LC OAD was plotted using measured data from the G.R.A.S. reference detector. The results suggested a light source with greater intensity and an LC cell with a different internal gap height, which were implemented in Section 3.4 and 4.4. The photolithographed LC cell design with a different gap height removed the ringing effect of the optical transmission bandgap. Finally, the experimental LC-enhanced photophone was created and successfully demonstrated the ability of CLC to improve the performance of a simple photophone.

V. Conclusions and Recommendations

This chapter is divided into two main sections and an overall summary. Section 5.1 combines the conclusions and recommendations for the two-factor and three-factor statistical analysis experiments. Section 5.2 covers the final two optoacoustic detection efforts. Each section includes a subsection with future recommendations.

5.1. Statistical Design of Liquid Crystal

The presented statistical design method was a precursor to designing ideal CLC features. Using the wealth of prior research, factors were chosen and tested to inform the design of LC for various applications. The two-factor experiment determined the dopant concentration of the CLC used in subsequent sensor designs. The three-factor experiment corroborated the results from the two-factor experiment as a proof-of-concept for future experimental factors. The strength of this method was the ability to find significant interactions as opposed to calculating the complex chemical and physical interactions that influenced the desired features of the optical bandgap.

5.1.1. Recommendations for Future Research

These initial results and analyses set the stage for other factors that could be investigated. Other possible main factors include LC cell gap height (per Section 4.1) intensity of the driving light (as indicated in Section 4.3), incident angle of measurement, time left in storage, and type of source light. Moreover, the interactions between some or all of these main factors increase the amount of experimental possibilities. Other statistical analysis methods may also be used to aid significant factor identification, such as,

67

additional test runs to increase replicates and implementing different mathematical models. The ANOVA statistical method is one of many tools that are available.

The underlying substrate LC is deposited on may also be a factor of interest. The preparation of an LC host material involves a polymer and micro-abrasions created by rubbing cloth (Section 2.1). Controlling the shape and periodicity of the substrate on a nanometer scale may improve desired features of the CLC optical resonance. Possible substrate configurations are shown in Fig. 29 below. This was attempted during this research using a Nanoscribe machine to create an LC cell, but was not reported due to difficulty in measuring the optical transmission spectrum.
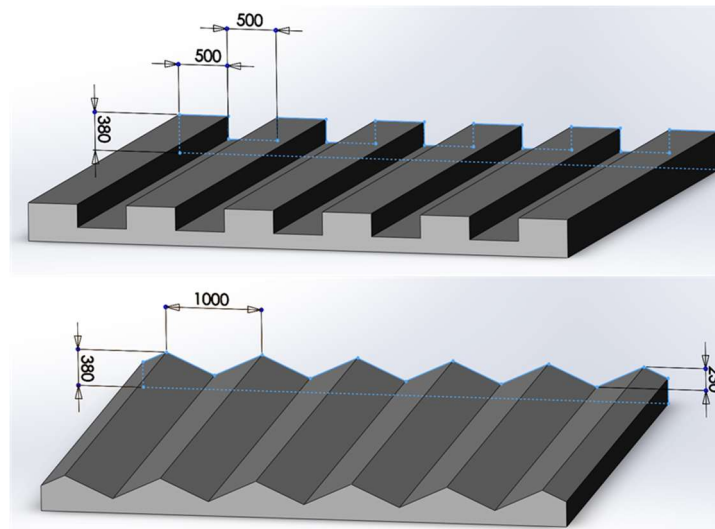
Figure 29. Two theoretical substrate designs for LC applications. The units are in nanometers. The depth of the square trench (top) is 230 nm, similar the sawtooth height (bottom).

5.2. Optoacoustic Detection using Liquid Crystal

This research investigated the possibility of employing geometry-independent liquid crystalline materials to detect broadband soundwaves. Exploration of this

www.manaraa.com

technology included the underlying theory and experimental validation of optoacoustic detection using liquid crystal. In theory, the low intensity of the light source reduced the useful detection limit, and the rigidity of the liquid crystal cell host significantly attenuated the sound pressures. As a result, an incremental experiment was conducted, which culminated in a photolithographed liquid crystal device used as a simple photophone. The increase of light modulation amplitude (peak-to-peak voltage) as seen by the photodetector was correlated to the increase of the bandgap edge slope. These results demonstrated that the optical transmission bandgap of cholesteric liquid crystal can inherently enhance an existing optoacoustic sensing device without the use of external electronic amplifiers.

5.2.1. *Recommendations for Future Research*

The LC cell constructed in Subsection 3.4.1 was an initial step toward an improved LC cell. Ideally, the apparatus that physically touches the LC must be an infinitesimally thin membrane. This will allow incident acoustic waves to impinge more directly to the LC molecules without experiencing acoustic absorption of the host cavity. In addition, a light source with greater intensity, such as a laser, can yield a greater response than that of the LC-enhanced photophone or commercial reference detector in this research. If broadband light is pursued in future research, it is recommended to develop a way to couple more light into a photodetector. In addition, other novel materials may also be used in a similar manner to create an optoacoustic detector, such as the photoluminescent qualities of quantum dots, and other light-emitting, or light-altering, materials.

The LC-enhanced photophone measurement described in 3.4.2 was confined to a single frequency. If a series of broadband frequencies, ranging from infrasound to

69

ultrasound, were launched and measured for both the glass and LC photophone, then one can obtain a series of comparisons between the glass and LC photophone amplitudes. If every glass photophone measurement was increased by the same factor as compared to the corresponding LC photophone measurement, then this would further support the enhancing abilities of cholesteric liquid crystal when used as an optoacoustic sensor. An extended literature review can aid the refinement of the design, such that a molecular LC-aided photophone can be realized.

5.3. Summary

This research pursued the development of an economical, compact, and sensitive liquid crystal-based acoustic sensor for use in a myriad of applications. The presented statistical design method highlights the limitless combinations of factors that enable the opportunity for anyone inside or out of this field to develop statistically-enhanced molecular designs of thin-film cholesteric liquid crystal for broad sensor applications. Liquid-crystalline materials undoubtedly exemplify a dynamic system that combines liquid-like softness, which is highly responsive to environmental changes, and controllable crystalline-like ordering that provides adjustable photonic bandgaps. This analysis and application of these material features significantly advance the utility of cutting-edge optoacoustic detector technologies and beyond.

Appendix A: MATLAB code for Reading Spectrometer Data

```matlab
 %Outputs: 1 figure with 2 plots, and 2 corresponding 'ExportData' variables
%reads spectrometer data from .txt file
    %.txt file must be in the same folder as this .m file

%Spectrometer model used: Ocean Optics FLAME-S-VIS-NIR-ES
%PC software application: OceanView (Spectroscopy Software with GUI)

range = [450 850 0 100];    % [xmin xmax ymin ymax], ranges for plot

%%plot 1st spectrum
%dlmread(filename, delimiter, row data start offset, column data start offset)
F1 = dlmread('C#34.txt','\t',14,0); %read data
W = F1(:,1);    %wavelength in nm
I = smoothdata(F1(:,2));    %intensity
% I = (F1(:,2)); %use this instead of above for not smoothed data
plot(W,I)
axis(range)
grid on
hold on
ExportData1 = [W,I];    %exports as two column variable

%%plot 2nd spectrum
F2 = dlmread('C#50_2.txt','\t',14,0);
W = F2(:,1);
I = smoothdata(F2(:,2));
% I = (F2(:,2)); %use this instead of above for not smoothed data
plot(W,I,'-r')
ExportData2 = [W,I];
```

71

Appendix B: MATLAB Code to Find Steepest Slope of a Transmission Spectrum

```
%This Code Outputs:
       %The steepest slope of amplitude vs wavelength
               %with units of [%transmission / nanometer]
       %Figure showing location of steepest slope

%Developed with great assistance from Capt Jonathan W. Smith.
%Spectrometer model used: Ocean Optics FLAME-S-VIS-NIR-ES
%PC software application: OceanView (Spectroscopy Software with GUI)

%% ----\/--Search Parameters--\/----
%Run code to find the range you want to clip the data at,
%then re-run with new range
xRange = [400 600]; %sets x-range for figure in nanometers
yRange = [40 90];    %sets y-range for figure in %transmission

XminValue = 450; %Min wavelength for slope test range
XmaxValue = 550; %Max wavelength for slope test range
xWin = 6;    %wavelength step-size of smallest "clean" section
%adjust if you want the program to ignore small/large
%bumps in the plot within this x-window size
%a value of 1 is ~=0.35 nm
%each x-value data point (row in the file)
%is separated by this amount
%% \/----\/--Input data--\/----\/
F1 = dlmread('FilenameOfData.txt','\t',14,0);
%file must be in the same folder as this code
%dlmread('filename', 'delimiter', row data start offset,
%column data start offset)
Vec1 = F1(:,1);      %Data, Wavelength in nm
Vec2 = (F1(:,2));      %Data, light intensity in %Transmission

% %% \/----\/--Test region defined from raw data--\/----\/
snipVec1 = Vec1(Vec1 > XminValue & Vec1 < XmaxValue);
%snipped wavelength input vector with correct range

IndeciesStartNewVec2 = find(Vec1 == snipVec1(1));
IndeciesEndNewVec2 = find(Vec1 == snipVec1(end));
snipVec2 = Vec2(IndeciesStartNewVec2:IndeciesEndNewVec2);
%snipped intensity vector with correct range

%% \/----\/--Iterates through finding steepest slope--\/----\/
%only iterates through test region!

Slope = 0;  %initialize ALL VARIABLES to ensure continuity between runs
SlopeLocation1 = 0;
SlopeLocation2 = 0;
TempSlopeLocation1 = 0;
TempSlopeLocation2 = 0;
TempSlope = 0;
stepTestSlopes = 0;
ptpSlope = 0;
```

72

```matlab
testStep1 = 0;
testStep2 = 0;

for r = 1 : (size(snipVec1,1)-(xWin-1))
%ends search based on snipped vector size and step size window

testStep1 = snipVec1(r : r+xWin-1);
%test step size taken from snipped wavlength vector
testStep2 = snipVec2(r : r+xWin-1);
%corresponding intensity vector
stepTestSlopes = zeros(1,xWin-1);
%initialize storage of point-to-point(ptp) slopes
for s = 1 : size(testStep1)-1
ptpSlope = (testStep2(s+1) - testStep2(s))./(testStep1(s+1)...
- testStep1(s));
stepTestSlopes(s) = ptpSlope;
end
if (all(stepTestSlopes(:) <= 0)) || (all(stepTestSlopes(:) >= 0))
%ensures data is a clean step, meaning, all incremental ptpslopes
%have the same sign (-/+). In other words the entire test step must
%be sloping sloping in the same direction. Ensures clean reading.

TempSlope = (snipVec2(r+xWin-1) - snipVec2(r))./(snipVec1(r+xWin-1)...
- snipVec1(r));
% finds slope. uses beginning and end of entire clean section
TempSlopeLocation1 = [snipVec1(r), snipVec1(r+xWin-1)];
%wavelength locations
TempSlopeLocation2 = [snipVec2(r), snipVec2(r+xWin-1)];
%intensity locations
%stores beginning of testStep in relation to the snipped vector

if abs(TempSlope) > Slope
%if temporary slope is greater than current saved slope

Slope = abs(TempSlope)  %save steepest slope
SlopeLocation1 = TempSlopeLocation1;
%save wavelength location (start/stop of step with steepest slope)
SlopeLocation2 = TempSlopeLocation2;
%save intensity corresponding values

else
end

else
end


end

%% \/----\/--Generate all plots--\/----\/----\/----\/
%Use this to find what wavelengths you want to clip at

figure(1)
hold on
plot(Vec1, Vec2,'c') %noise/original
```

73

```matlab
plot(snipVec1, snipVec2,'k') %slope test region
plot(SlopeLocation1, SlopeLocation2,'r*') %start/stop of steepest slope
axis([xRange yRange])    %Adjusts scale based on search parameters
title('LC Optical Spectrum')
xlabel('Wavelength')
ylabel('% Transmission')
legend('Original Data','Slope Test Region','Start/Stop of Steepest Slope',...
'location','southeast')
grid on
```

www.manaraa.com

Appendix C: MATLAB code for Reading Oscilloscope Data

```matlab
%Outputs: 1 figure, and 2 corresponding 'ExportData' variables

%reads data from .csv files from Agilent Inifiniium MSO8104A oscilloscope
%.csv file must be in the same folder as this .m file

%% 1st set of data
% ----vvvv---SET PARAMETERS 1----vvvv---
Filename = 'FILENAME1.csv';
ampConv = 1; %outputs amplitude in [1 = V, 1E3 = mV, etc]
timeConv = 1; %outputs amplitude in [1 = s, 1E3 = ms, etc]
colOffset = 3; %column offset for target data column of .csv file
    %(1 = 1st column, 2 = 2nd column, etc.)
%use screenshot of oscilloscope and .csv to relate channels/columns

% ----vvvv---interpretation algorithm 1----vvvv---
F1 = dlmread(Filename,',',23,0); %store time and voltage X & Y
    %points from .csv file
%dlmread(filename, delimiter, row data start offset, col data start offset)
X = F1(:,1);    %raw X data
Y = F1(:,colOffset);    %raw Y data
Xinc = dlmread(Filename,',',[8 1 8 1]); %gets Xinc for this file
ind = 0 : length(X)-1;  %creates indices for each row, 0, 1, 2, ... to end
    %of X value vector
Time = ind .* Xinc.* timeConv;  %s, time
Ampl = smoothdata(Y .* ampConv);    %V, voltage

% ----vvvv---Plot 1----vvvv---
figure(1)
plot(Time,Ampl)
% plot(Time,smoothdata(Ampl))  %smoothens data with moving window average

xlabel('Time (s)')
ylabel('Amplitude (V)')
hold on
grid on

ExportData1 = [Time' , Ampl];

%% 2nd set of data to compare
%----vvvv---SET PARAMETERS 2----vvvv---
Filename = 'FILENAME2.csv';
ampConv = 1; %outputs amplitude in [1 = V, 1E3 = mV, etc]
timeConv = 1; %outputs amplitude in [1 = s, 1E3 = ms, etc]
colOffset = 6; %offset for intended data column
    %(1 = 1st column, 2 = 2nd column, etc.)
%use screenshot of oscilloscope and .csv to remember channels/columns

% ----vvvv---interpretation algorithm 2----vvvv---
F1 = dlmread(Filename,',',23,0); %store time and voltage X & Y
```

75

```matlab
    %points from .csv file
X = F1(:,1);      %raw X data
Y = F1(:,colOffset);      %raw Y data
Xinc = dlmread(Filename,',',[8 1 8 1]); %gets Xinc for this file
ind = 0 : length(X)-1;  %creates indices for each row, 0, 1, 2, ... to end
    %of X value vector
Time = ind .* Xinc.* timeConv;  %s, time
Ampl = Y .* ampConv;      %V, voltage

% ----vvvv---Plot 2----vvvv---
figure(1)
plot(Time,Ampl)
% plot(Time,smoothdata(Ampl))  %smoothens data with moving window average

ExportData2 = [Time' , Ampl];
```

Appendix D: Process Follower for SF 1818 Photoresist

1. Turn on Hotplate and set to 110 °C

    SOLVENT CLEAN OF SUBSTRATE

2. Set Spinner Speed at 500 RPM

3. Set Spinner Time for 300 sec

4. Place substrate on the appropriate chuck and press VAC

5. Press start and perform the following using the stop watch

    a. 30 sec acetone rinse

    b. 30 sec Methanol rinse

    c. 30 sec Isopropyl or DI water rinse

    d. 30 sec dry with Nitrogen

6. Dehydrate bake on 100 °C Hotplate for 2 min

7. After 2 min remove and allow substrate to cool for 30 sec

    PHOTORESIST COATING OF SUBSTRATE

8. Set Spinner Speed at 5,000 RPM

9. Set Spinner Time for 30 sec

10. Set Ramp speed at 500 RPM

11. Place substrate on the appropriate chuck and press VAC

12. Flood substrate with 1818 photoresist

13. Start 30 sec spin at 4000 RPM

14. When spinner stops remove substrate and place on 100 ° C hotplate for 2 min bake

15. After 2 min remove substrate and allow to cool

16. Inspect substrate for even coating of photoresist before performing Photolithography

Appendix E: Process follower for Photolithography

1. Turn on the Deep UV controller (not the UV light) to allow for 15 min warm-up

2. Set the Deep UV controller time to 5 min

3. Set the pre-photoresist-coated substrate underneath the

4. Set and align the mask on top of the substrate

5. Turn on the Deep UV

6. When the Deep UV turns off, remove the substrate and mask

7. Set only the substrate in a 5:1 ratio bath of DI water and NaOH (Shipley 351), respectively

    a. Carefully agitate the bath, then remove the substrate after 40 sec

8. Rinse with DI water and dry with nitrogen gas

9. Inspect the sample. If photoresist remains, repeat steps 2-9 with a new substrate and increase the Deep UV time by 5 min

Appendix F: Two-Factor Individual Slope Measurements

Cell ID #	Temperature	Dopant (%wt)	Replicate #	|Slope| (%trans. / nm)	Avg (%trans. / nm)
14	Room	0	1	0	0.9042
				1.3116	
				1.401	
15	Room	1.08	1	2.5479	3.246267
				3.8015	
				3.3894	
16	Room	2.05	1	3.3663	3.937733
				4.3006	
				4.1463	
17	Room	2.56	1	3.2887	3.433733
				3.4729	
				3.5396	
18	103.9°C	0	1	1.2666	0.887
				0.7386	
				0.6558	
19	103.9°C	1.08	1	4.0058	4.076167
				4.7636	
				3.4591	
20	103.9°C	2.05	1	4.942	4.713867
				5.2815	
				3.9181	
21	103.9°C	2.56	1	3.4153	3.062767
				3.0503	
				2.7227	
22	Room	0	2	0.9182	0.7142
				1.2244	
				0	
23	Room	1.08	2	3.4994	3.2219
				3.31	
				2.8563	
24	Room	2.05	2	4	3.840067
				4.2484	
				3.2718	
25	Room	2.56	2	2.5418	2.577633
				2.6339	

79

				2.5572	
26	103.9°C	0	2	0.5968	0.6528
				1.3616	
				0	
27	103.9°C	1.08	2	2.6733	2.274367
				1.513	
				2.6368	
28	103.9°C	2.05	2	3.2392	2.664167
				2.5375	
				2.2158	
29	103.9°C	2.56	2	3.4897	3.033467
				2.1417	
				3.469	

80

Appendix G: Three-Factor Individual Slope Measurements

Rdm order	std order	Temp	Pressure	Dopant / Cell ID	Replicate	|Slope| (%trans. / nm)	Avg Slope (%trans. / nm)
12	1	55	vac	C#17	1	4.2381	4.4021
						3.9543	
						5.0139	
14	2	55	vac	C#15	1	5.0878	4.1792
						4.0568	
						3.393	
10	3	55	room	C#17	1	5.284	5.6918
						5.5762	
						6.2152	
5	4	55	room	C#15	1	4.9387	5.121467
						5.2649	
						5.1608	
16	5	22	vac	C#17	1	5.7338	5.0559
						4.4172	
						5.0167	
6	6	22	vac	C#15	1	6.8166	6.6638
						5.6235	
						7.5513	
7	7	22	room	C#17	1	6.9499	4.926367
						4.0485	
						3.7807	
8	8	22	room	C#15	1	7.506	5.743167
						3.8621	
						5.8614	
2	9	55	vac	C#25	2	4.7658	4.257867
						3.9241	
						4.0837	
3	10	55	vac	C#23	2	4.9789	5.3585
						5.9008	
						5.1958	
11	11	55	room	C#25	2	4.3928	4.893433
						5.1783	
						5.1092	
1	12	55	room	C#23	2	7.193	4.612233
						1.5387	
						5.105	

81

13	13	22	vac	C#25	2	5.256	4.560133
						4.1606	
						4.2638	
9	14	22	vac	C#23	2	5.7155	5.657033
						5.462	
						5.7936	
4	15	22	room	C#25	2	5.5619	5.001267
						5.655	
						3.7869	
15	16	22	room	C#23	2	5.5455	6.229533
						5.3593	
						7.7838	

Bibliography

[1]   M. A. Welsh, "America's Air Force: A Call to the Future," Washington, D.C., 2014.

[2]   J.-B. Ihn and F.-K. Chang, "Pitch-catch Active Sensing Methods in Structural Health Monitoring for Aircraft Structures," *Struct. Heal. Monit. An Int. J.*, vol. 7, no. 1, pp. 5–19, Mar. 2008.

[3]   E. S. Posmentier, "1- to 16-Hz infrasound associated with clear air turbulence predictors," *J. Geophys. Res.*, vol. 79, no. 12, pp. 1755–1760, Apr. 1974.

[4]   J. P. Mutschlecner and R. W. Whitaker, "Infrasound from earthquakes," *J. Geophys. Res.*, vol. 110, no. D1, p. D01108, Jan. 2005.

[5]   D. F. Rivera and R. Bansal, "Towed antennas for US submarine communications: a historical perspective," *IEEE Antennas Propag. Mag.*, vol. 46, no. 1, pp. 23–36, Feb. 2004.

[6]   D. P. Drob, J. M. Picone, and M. Garcés, "Global morphology of infrasound propagation," *J. Geophys. Res. Atmos.*, vol. 108, no. D21, Nov. 2003.

[7]   O. T. Inan *et al.*, "Ballistocardiography and Seismocardiography: A Review of Recent Advances," *IEEE J. Biomed. Heal. Informatics*, vol. 19, no. 4, pp. 1414–1427, Jul. 2015.

[8]   A. Fenster, D. B. Downey, and H. N. Cardinal, "Three-dimensional ultrasound imaging," *Phys. Med. Biol.*, vol. 46, no. 5, pp. R67–R99, May 2001.

[9]   L. V Wang and S. Hu, "Photoacoustic tomography: in vivo imaging from organelles to organs.," *Science*, vol. 335, no. 6075, pp. 1458–62, Mar. 2012.

[10]   G. P. Crawford, A. Schenning, and D. J. Broer, *Liquid Crystal Sensors*. Taylor & Francis Group, 6000 Broken Sound Parkway NW, Suite 300, Boca Raton, FL 33487-2742: CRC Press, 2017.

[11]   L. Wang, A. M. Urbas, and Q. Li, "Nature-Inspired Emerging Chiral Liquid Crystal Nanostructures: From Molecular Self-Assembly to DNA Mesophase and Nanocolloids," *Adv. Mater.*, p. 1801335, Aug. 2018.

[12]   K. S. Shim *et al.*, "Temperature-independent pitch invariance in cholesteric liquid

83

crystal," *Opt. Express*, vol. 22, no. 13, p. 15467, Jun. 2014.

[13]   H. K. Bisoyi and Q. Li, "Light-Directing Chiral Liquid Crystal Nanostructures: From 1D to 3D," *Acc. Chem. Res.*, vol. 47, no. 10, pp. 3184–3195, Oct. 2014.

[14]   L. Wang and Q. Li, "Stimuli-Directing Self-Organized 3D Liquid-Crystalline Nanostructures: From Materials Design to Photonic Applications," *Adv. Funct. Mater.*, vol. 26, no. 1, pp. 10–28, Jan. 2016.

[15]   L. Chen, Y. Li, J. Fan, H. K. Bisoyi, D. A. Weitz, and Q. Li, "Photoresponsive Monodisperse Cholesteric Liquid Crystalline Microshells for Tunable Omnidirectional Lasing Enabled by a Visible Light-Driven Chiral Molecular Switch," *Adv. Opt. Mater.*, vol. 2, no. 9, pp. 845–848, Sep. 2014.

[16]   J. Beeckman, K. Neyts, and P. J. M. Vanbrabant, "Liquid-crystal photonic applications," *Opt. Eng.*, vol. 50, no. 8, p. 081202, Aug. 2011.

[17]   J. Stöhr and M. G. Samant, "Liquid crystal alignment by rubbed polymer surfaces: a microscopic bond orientation model."

[18]   X. Qiao, X. Zhang, Y. Guo, S. Yang, Y. Tian, and Y. Meng, "Boundary layer viscosity of CNT-doped liquid crystals: effects of phase behavior," *Rheol. Acta*, vol. 52, no. 10–12, pp. 939–947, Nov. 2013.

[19]   Q. Ni, T. Marschke, S. Steele, N. Seyed, and N. B. Crane, "Studying of Contact Angle Friction and Contact Angle Hysteresis (CAH) Though Force Measurements," in *Volume 7: Fluids and Heat Transfer, Parts A, B, C, and D*, 2012, p. 721.

[20]   F. Reinitzer, "Beiträge zur Kenntniss des Cholesterins," *Monatshefte für Chemie - Chem. Mon.*, vol. 9, no. 1, pp. 421–441, Dec. 1888.

[21]   S. Pieraccini, S. Masiero, A. Ferrarini, and G. Piero Spada, "Chirality transfer across length-scales in nematic liquid crystals: fundamentals and applications," *Chem. Soc. Rev.*, vol. 40, no. 1, pp. 258–271, Dec. 2011.

[22]   J. Stöhr and M. G. Samant, "Liquid crystal alignment by rubbed polymer surfaces: a microscopic bond orientation model," *J. Electron Spectros. Relat. Phenomena*, vol. 98–99, pp. 189–207, Jan. 1999.

[23]   B. C. Jiang *, C.-C. Wang, and H.-C. Liu, "Liquid crystal display surface uniformity

84

defect inspection using analysis of variance and exponentially weighted moving average techniques," *Int. J. Prod. Res.*, vol. 43, no. 1, pp. 67–80, Jan. 2005.

[24] M. Mitov and N. Dessaud, "Going beyond the reflectance limit of cholesteric liquid crystals," *Nat. Mater.*, vol. 5, no. 5, pp. 361–364, May 2006.

[25] D. W. Schindel, D. A. Hutchins, Lichun Zou, and M. Sayer, "The design and characterization of micromachined air-coupled capacitance transducers," *IEEE Trans. Ultrason. Ferroelectr. Freq. Control*, vol. 42, no. 1, pp. 42–50, Jan. 1995.

[26] H. Nan *et al.*, "Non-contact thermoacoustic detection of embedded targets using airborne-capacitive micromachined ultrasonic transducers," *Appl. Phys. Lett.*, vol. 106, no. 8, p. 084101, Feb. 2015.

[27] S. T. Hansen, B. J. Mossawir, A. Sanli Ergun, F. Levent Degertekin, and B. T. Khuri-Yakub, "Air-coupled nondestructive evaluation using micromachined ultrasonic transducers," in *1999 IEEE Ultrasonics Symposium. Proceedings. International Symposium (Cat. No.99CH37027)*, 1999, vol. 2, pp. 1037–1040.

[28] R. G. M. Kolkman *et al.*, "Feasibility of noncontact piezoelectric detection of photoacoustic signals in tissue-mimicking phantoms," *J. Biomed. Opt.*, vol. 15, no. 5, p. 055011, 2010.

[29] A. J. Bedard and T. M. Georges, "Atmospheric Infrasound," *Phys. Today*, vol. 53, no. 3, pp. 32–37, Mar. 2000.

[30] I. Ladabaum, Xuecheng Jin, H. T. Soh, A. Atalar, and B. t. Khuri-Yakub, "Surface micromachined capacitive ultrasonic transducers," *IEEE Trans. Ultrason. Ferroelectr. Freq. Control*, vol. 45, no. 3, pp. 678–690, May 1998.

[31] L. Jakevičius and A. Demčenko, *Ultrasound attenuation dependence on air temperature in closed chambers*, vol. 63, no. 1. Mintis, 1969.

[32] R. E. Green, "Non-contact ultrasonic techniques," *Ultrasonics*, vol. 42, no. 1–9, pp. 9–16, Apr. 2004.

[33] W. Manthey, N. Kroemer, and V. Magori, "Ultrasonic transducers and transducer arrays for applications in air," *Meas. Sci. Technol.*, vol. 3, no. 3, pp. 249–261, Mar. 1992.

[34] G. Rousseau, A. Blouin, and J.-P. Monchalin, "Non-contact photoacoustic tomography and ultrasonography for tissue imaging," *Biomed. Opt. Express*, vol. 3, no. 1, p. 16, Jan. 2012.

[35] X. L. Deán-Ben, G. A. Pang, F. Montero de Espinosa, and D. Razansky, "Non-contact optoacoustic imaging with focused air-coupled transducers," *Appl. Phys. Lett.*, vol. 107, no. 5, p. 051105, Aug. 2015.

[36] A. G. Bell, "The Photophone," *Science (80-.).*, vol. 1, no. 11, pp. 130–134, 1880.

[37] S. Buzzelli, B. Catania, D. Gagliardi, and F. Tosco, "Optical fibre field experiments in Italy: COS1, COS2 and COS3/FOSTER," in *International Conference on Communications*, 1980, pp. 38–3.

[38] J. D. Hamilton, T. Buma, M. Spisar, and M. O'Donnell, "High frequency optoacoustic arrays using etalon detection," *IEEE Trans. Ultrason. Ferroelectr. Freq. Control*, vol. 47, no. 1, pp. 160–169, Jan. 2000.

[39] K. H. Kim *et al.*, "Air-coupled ultrasound detection using capillary-based optical ring resonators," *Sci. Rep.*, vol. 7, no. 1, p. 109, Dec. 2017.

[40] H. A. (Hugh A. Macleod, *Thin-film optical filters*. CRC Press/Taylor & Francis, 2010.

[41] P. C. Beard, F. Pérennès, E. Draguioti, and T. N. Mills, "Optical fiber photoacoustic–photothermal probe," *Opt. Lett.*, vol. 23, no. 15, p. 1235, Aug. 1998.

[42] S. Preisser *et al.*, "All-optical highly sensitive akinetic sensor for ultrasound detection and photoacoustic imaging," *Biomed. Opt. Express*, vol. 7, no. 10, p. 4171, Oct. 2016.

[43] Cheng Zhang, Sung-Liang Chen, Tao Ling, and L. J. Guo, "Review of Imprinted Polymer Microrings as Ultrasound Detectors: Design, Fabrication, and Characterization," *IEEE Sens. J.*, vol. 15, no. 6, pp. 3241–3248, Jun. 2015.

[44] H. Li, B. Dong, Z. Zhang, H. F. Zhang, and C. Sun, "A transparent broadband ultrasonic detector based on an optical micro-ring resonator for photoacoustic microscopy," *Sci. Rep.*, vol. 4, no. 1, p. 4496, May 2015.

[45] C. Chao, S. Ashkenazi, S. Huang, M. O'Donnell, and L. Guo, "High-frequency

ultrasound sensors using polymer microring resonators," *IEEE Trans. Ultrason. Ferroelectr. Freq. Control*, vol. 54, no. 5, pp. 957–965, May 2007.

[46] T. Ling, S.-L. Chen, and L. J. Guo, "Fabrication and characterization of High Q polymer micro-ring resonator and its application as a sensitive ultrasonic detector," *Opt. Express*, vol. 19, no. 2, p. 861, Jan. 2011.

[47] S. M. Leinders *et al.*, "A sensitive optical micro-machined ultrasound sensor (OMUS) based on a silicon photonic ring resonator on an acoustical membrane," *Sci. Rep.*, vol. 5, no. 1, p. 14328, Nov. 2015.

[48] G. N. de Brabander, J. T. Boyd, and G. Beheim, "Integrated optical ring resonator with micromechanical diaphragms for pressure sensing," *IEEE Photonics Technol. Lett.*, vol. 6, no. 5, pp. 671–673, May 1994.

[49] M. V. Chistiakova and A. M. Armani, "Photoelastic ultrasound detection using ultra-high-Q silica optical resonators," *Opt. Express*, vol. 22, no. 23, p. 28169, Nov. 2014.

[50] J. M. Ward, N. Dhasmana, and S. Nic Chormaic, "Hollow core, whispering gallery resonator sensors," *Eur. Phys. J. Spec. Top.*, vol. 223, no. 10, pp. 1917–1935, Sep. 2014.

[51] B. Dong *et al.*, "Isometric multimodal photoacoustic microscopy based on optically transparent micro-ring ultrasonic detection," *Optica*, vol. 2, no. 2, p. 169, Feb. 2015.

[52] D. C. Montgomery, *Design and Analysis of Experiments*, 9th ed. John Wiley & Sons, Inc., 2017.

Vita

Captain Michael T. Dela Cruz graduated from St. Mary's University with a Bachelor's degree in Electrical Engineering in 2011. He was commissioned through Officer Training School as a Second Lieutenant in the United States Air Force in March 2014 with a job specialty in Developmental Engineering. His first assignment was as a Guidance System Modernization Engineer in the Intercontinental Ballistic Missile (ICBM) Systems Directorate, followed by his second assignment as a Reentry Vehicle Applications Program Manager in the same directorate. Here he received the 2017 Brent Scowcroft Award for Individual Achievement in ICBM Acquisitions & Sustainment. In August 2017, he began his Master's degree in Electrical Engineering through the Engineering and Management School at the Air Force Institute of Technology. Upon graduation he will be assigned to the Air Force Operational Test and Evaluation Center.

REPORT DOCUMENTATION PAGE

The public reporting burden for this collection of information is estimated to average 1 hour per response, including the time for reviewing instructions, searching existing data sources, gathering and maintaining the data needed, and completing and reviewing the collection of information. Send comments regarding this burden estimate or any other aspect of this collection of information, including suggestions for reducing the burden, to Department of Defense, Washington Headquarters Services, Directorate for Information Operations and Reports (0704-0188), 1215 Jefferson Davis Highway, Suite 1204, Arlington, VA 22202-4302. Respondents should be aware that notwithstanding any other provision of law, no person shall be subject to any penalty for failing to comply with a collection of information if it does not display a currently valid OMB control number.
PLEASE DO NOT RETURN YOUR FORM TO THE ABOVE ADDRESS.

1. REPORT DATE *(DD-MM-YYYY)*	2. REPORT TYPE	3. DATES COVERED *(From - To)*

4. TITLE AND SUBTITLE

5a. CONTRACT NUMBER

5b. GRANT NUMBER

5c. PROGRAM ELEMENT NUMBER

6. AUTHOR(S)

5d. PROJECT NUMBER

5e. TASK NUMBER

5f. WORK UNIT NUMBER

7. PERFORMING ORGANIZATION NAME(S) AND ADDRESS(ES)

8. PERFORMING ORGANIZATION REPORT NUMBER

9. SPONSORING/MONITORING AGENCY NAME(S) AND ADDRESS(ES)

10. SPONSOR/MONITOR'S ACRONYM(S)

11. SPONSOR/MONITOR'S REPORT NUMBER(S)

12. DISTRIBUTION/AVAILABILITY STATEMENT

13. SUPPLEMENTARY NOTES

14. ABSTRACT

15. SUBJECT TERMS

16. SECURITY CLASSIFICATION OF:			17. LIMITATION OF ABSTRACT	18. NUMBER OF PAGES	19a. NAME OF RESPONSIBLE PERSON
a. REPORT	b. ABSTRACT	c. THIS PAGE			
					19b. TELEPHONE NUMBER *(Include area code)*